# Engineering physico-chemical interactions across drug delivery, agriculture and carbon capture

Vishnu Jayaprakash

B.S, University of California, Berkeley (2015)
M.S, Massachusetts Institute of Technology (2019)

Submitted to the Department of Mechanical Engineering
in Partial Fulfillment of the Requirements for the Degree of

Doctor of Philosophy in Mechanical Engineering

at the

MASSACHUSETTS INSTITUTE OF TECHNOLOGY

February 2022



Signature of Author: _____
Department of Mechanical Engineering
January, 7th 2022

Certified by: _____
Kripa K. Varanasi
Professor, Department of Mechanical Engineering
Thesis Supervisor

Accepted by: _____
Nicolas Hadjiconstantinou
Professor of Mechanical Engineering
Graduate Officer

# Engineering physico-chemical interactions across drug delivery, agriculture and carbon capture

by

Vishnu Jayaprakash

Submitted to the Department of Mechanical Engineering
on January 7th, 2022 in Partial Fulfillment of the
Requirements for the Degree of

Doctor of Philosophy in Mechanical Engineering

# Abstract

The interface between two phases often limits the efficiency of several phenomena. In drug delivery, viscous formulations are difficult to inject through medical needles as the no-slip boundary condition between the needle and the viscous drug product greatly resists fluid flow. In agriculture, the inherent water repellency of plant surfaces causes pesticide sprays to bounce off, resulting in enormous waste and environmental pollution. In post-combustion carbon capture, absorbing gaseous $CO_2$ into liquids remains prohibitively expensive as reaction rates are limited by the low interfacial areas between the flue gas and absorbents in current systems. This work explores how introducing new interfaces or interfacial forces can help solve these three challenges. First, we demonstrate viscosity agnostic injectability of drug formulations through needles using core annular flows, where the transport of a highly viscous fluid through a needle is enabled via coaxial lubrication by a less viscous fluid. Second, by cloaking spray droplets in minute quantities of plant oils ($\leq$ 1wt%), we enhance energy dissipation during droplet impact on hydrophobic surfaces and demonstrate a 5x reduction in pesticide waste on a variety of plant leaves. Finally, mist-scale droplets and space charge injection are used to enhance interfacial areas in $CO_2$ absorption and develop a carbon capture system that could lead to a 2.6x reduction in plant capital costs.

Thesis Supervisor: Kripa K. Varanasi
Title: Professor, Department of Mechanical Engineering

# Acknowledgements

First and foremost, I would like to thank my advisor Prof. Kripa Varanasi who has taught me so much more than I imagined possible during my time at MIT and who has made all of this work possible. It is impossible to overstate the positive influence that Kripa has had on my life, outlook and growth over the past few years. Kripa was a key part of my decision to pursue a doctoral degree and his vision for the work we could do together motivated me from the day I joined his lab in late 2016. His ability to find impactful problems, his philosophy of building solutions by establishing fundamental scientific frameworks and his focus on bringing products to market are all things that have inspired me throughout my work. He has taught me new ways to focus on the right details, and communicate effectively and I cherish every meeting we have had, which were great opportunities for brainstorming and scientific debate. Through his guidance and advice, I have had the rare opportunity to work on impactful issues that I care deeply about, with some of the most influential people in the world. It has been one of the greatest pleasures of my life to work with him and I'm extremely excited that our passion for entrepreneurship will allow us to continue working together for over the coming years.

I also thank Professor Ming Guo and Professor Paulo Lozano for serving on my doctoral committee, and for their insights, feedback and advice.

I was incredibly lucky to be in an exceptionally talented, kind and fun-loving lab group. It has been a great pleasure to form deep friendships with all of the members of the Varanasi group, past and present. None of this work would have been possible without the input, insights, feedback and effort of all of the lab-mates I've had the pleasure of working with. I want to thank Sreedath Panat, Simon Rufer and Maxime Costalonga not only for their invaluable contributions but also for being great friends. I want to thank Caroline McCue, whose friendship and support I have leaned on heavily and Samantha McBride whose advice and sense of humor have always improved my day. Jack Lake, Victor Leon, Bert Vanderyedt, Baptiste LeBlanc, Karim Khalil, Alex Trias, Divya Panchanathan, David Kang, Somayajulu Dhulipala, Dan Soto, Leonid Rapoport, Valentina Negri, Ingrid Guga, Maher Damak, Tal Joseph, Fabian Dickhardt, and all the other Varanasi group members I have had the privilege of working with, thank you for making the last 5 and a half years amazing!

During my doctoral work, I have had the privilege of working with and learning from many people in the MIT community. It is impossible to thank all of them by name, but I would like to thank all the professors who taught me. Dan Gilbert, Paul and the staff at the LMP and Edgerton machine shops, the Makerworks volunteers and the MechE

administrators, thank you all so much for making my time at MIT one of the most enjoyable and memorable periods of my life.

I want to thank all the members of DEI task force: Prof. Asegun Henry, Prof. Cullen Buie, Dr. Dawn Wendell, Katey Stewart, Yadira Rivera, Bryan Nance, Fiona Grant, Dr. Dan Oropeza, Jonathan Tagoe, Daniel Diaz, Stacey Igwe, the task force's members at large body and everyone in the MIT community who engaged with our taskforce's efforts. All of you have been a source of inspiration and invaluable support over the past two years. I know we still have lot of work to do but it has been one of the greatest honors of my life to work with all of you on improving DEI in our department at MIT.

To all the members of GAME and the GAME DEI working group, it's been a blast to be able to work with all of you. We have made memories that will last a lifetime and I thank each and every one of you for the work you do and the quality of your company.

On a personal note, I would like to thank my parents, Bhavani and Rajan Jayaprakash as I can very comfortably say that I would not be where I am today without their unconditional and selfless love and support. They have been a source of inspiration and motivation throughout my life. I would like to thank my brother, Agnishwar Jayaprakash for truly being the best older brother anyone could ask for. You have been my role model since we were kids and your love and support has kept me going through it all. I also wish to thank my partner Shivya Bansal in particular for her tremendous support over the past 6 years. Thank you for always being there for me, being incredibly patient, inspiring me and for being a source of never-ending joy in my life.

I also wish to acknowledge all of the friends, and even acquaintances, I have met during my time at MIT. I have never been in an environment with so many positive, kind, and supportive people, and I am grateful to everyone in the Mechanical Engineering Department and beyond who have made my PhD experience what it was.

*To my mother, who has been my greatest advocate and my bastion of love and support*

# Contents

# List of Figures

# List of Tables

# Introduction

*Interfaces and the challenges of leveraging them*

Interfaces are the boundaries between different phases of matter or the area of contact between two or more distinct materials. They are prime locations at which a wide range of exchanges: including heat, mass, momentum, charge and chemical exchange can occur. These transfers across interfaces can happen over various length and time-scales and have profound outcomes on the behavior of systems. Given their influence, extensive work has been done to enhance or limit exchanges, reactions and interactions at interfaces. Such interfacial engineering is challenging as several properties need be tuned to achieve a desired result. A number of these properties or levers could have conflicting effects and practical limitations have to be considered in finding compromises. This leads to extensive work in balancing the various physical and chemical properties and interactions in systems to find optimums.

*Fluidic transport through enclosed geometries*

Enabling and easing the transport of liquids through enclosed pipes has been an engineering objective for centuries, be it in water or oil pipelines spanning hundreds of miles or in laptop heat exchangers that span a few hundred microns. Typically, the liquid is driven by a pressure gradient and must overcome the hydrodynamic resistance presented by flow through the solid pipe. While this resistance is a function of pipe geometry and the rheological properties of the fluid, the condition that enforces the resistance is the no-slip boundary criterion at the interface between the liquid and the solid wall. To minimize the pressure gradient required to achieve a specific flow rate through a pipe of set dimensions, a number of approaches have been explored. If we consider Newtonian fluids for this example, reducing the viscosity of the fluid via additives would allow for easier transport. From an interfacial perspective, replacing the no-slip boundary condition with a slip length condition through the use of superhydrophobic or liquid infused surfaces could also ease transport. However, if the fluid of interest is a drug product that's carefully engineered to generate an immune response, changing its chemical composition or its inherent viscosity via additives would be extremely challenging. Secondly, if the viscosity of the drug product is so high that the benefits offered by surface modification aren't sufficient to allow the liquid to flow through needles in the time it takes for a typical injection (a few seconds), new methods to overcome the constraints of the no-slip boundary condition are needed.

*Droplet impact and retention on surfaces*

The impact, coating and rebound behavior of droplets on surfaces is of-interest in the study and optimization of a variety of natural and industrial processes like rain, thermal spraying, paint coating, agricultural spraying and printing. During impact on solid surfaces which occur over a few milliseconds, Newtonian liquid droplets undergo expansion that is driven by inertial forces and retraction that is driven by surface tension and the viscosity of the droplet. In fact, a variety of surface properties such as surface energy, micro and nano-texture and elasticity and droplet properties like surface tension, viscosity, density, droplet size and impact velocity can all affect whether an impacting droplet will bounce-off or stick on a solid surface. In the context of agricultural sprays, the limiting interface is the contact area between the water droplet that is carrying agrochemical products and the hydrophobic or superhydrophobic plant surface. Spray retention on leaves needs to be promoted without having any degree of influence over the solid surface as it is difficult to control the inherent properties of plants. As such, a variety of approaches involving additives like surfactants, polymers, and charge carriers have been proposed but maximizing cost effective agrochemical spray retention while having minimal impacts on plant, environmental and human health is still an open challenge.

*Absorption of a gases into liquids*

Absorption is the process through which molecules of one phase enter a bulk of another. This behavior is governed by numerous physical, chemical, electronic and electrostatic properties ranging from temperature and pressure to chemical concentrations and surface charge. In the context of carbon capture, the goal is to absorb gaseous $CO_2$ molecules into a liquid that usually contains a chemical catalyst. The boundary between the gas and liquid can once again present a limiting interface for this reaction and increasing the contact area between these two phases can increase the efficiency of absorption. However, increasing contact areas in an economically feasible way can be extremely challenging if the requirement is to capture $CO_2$ from the high flow rate (approximately 800 kg/s) exhaust streams of power plants.

*Thesis outline*

In this work, we will explore how engineering the physico-chemical interactions cat interfaces can unlock efficiency enhancements. Specifically, we will look at the benefit of introducing new interfaces and interfacial forces for three distinct applications. In chapter 1, we tackle the problem of injecting a new generation of highly viscous drug formulations that can have viscosities as high as 500cP through medical needles. The goal of our work is to develop a device that uses core annular flows - where the transport of a viscous fluid is enabled by coaxial lubrication by a less viscous fluid - to enable the injection of viscous biologic drug formulations. To achieve this, we first report the flow regimes observable in

such a device and establish a regime map to indicate the flow rates and viscosity ratios at which core annular flow can be sustained in a needle. We then quantify the corresponding pressure reduction and compare our measurements with theoretical predictions. We design, fabricate, and test a first-generation double-barreled prototype syringe to exhibit the capability of this technique to inject high concentration drug formulations. Finally, we examine buoyancy effects to inform the development of a viscosity agnostic injection technique.

In chapter 2, we tackle the problem of droplets from agrochemical sprays bouncing off of hydrophobic plant surfaces. By cloaking the droplets in minute quantities of plant oils ($\leq$ 1wt%), we promote energy dissipation and enhance droplet retention on hydrophobic surfaces. To fully understand this technique's potential to enhance droplet retention, we study it systematically with two types of nanoengineered superhydrophobic surfaces. These surfaces represent the most extreme case that agricultural sprays can encounter. Studying enhancements in droplet retention in this extreme case provide a conservative benchmark for our methodology. We examine droplet impact dynamics at a variety of agriculturally relevant spray velocities and Weber numbers and systematically study the effect of cloaking with different oils of varying surface tension and viscosity. We explore the effect of oil fraction and present a simple energy state framework to explain the rebound suppression observed with oil cloaked droplets. Finally, we then test a practical embodiment of this system and demonstrate significant improvements in spray retention on nanoengineered superhydrophobic surfaces and vegetable crop leaves.

In chapter 3, we explore how $CO_2$ absorption into liquid media in post-combustion carbon capture systems can be improved by enhancing the interfacial area between gaseous $CO_2$ and a liquid absorbent. We propose a two-stage system to practically leverage the advantages offered by micron-scale droplets. In the first – absorption stage, we propose using absorbent droplets with diameters between 15 and 50 µm, which would allow our system to achieve up to a 280-fold increase to the interfacial area available between the absorbent and the gas compared to conventional packed bed absorption reactors. Given that such droplets will be entrained by the gas flow exhausting from industrial power plants, we propose a second – electrostatic droplet capture stage to arrest the entrained liquid drops. Specifically, by utilizing a corona discharge, we will charge the mist-scale droplets on the and introduce an electrical force that will drive them to a collector from where the liquid absorbent can be collected, processed and recirculated. We develop and test a scaled down version of our two-stage design. For the first stage of our system, we match the gas flux of industrial absorber units and study the effect of input $CO_2$ and catalyst concentration on $CO_2$ capture efficiency. For the second stage, we explore the droplet capture efficiency of a scaled down electrostatic system as a function of gas flow

rate and the electric field strength. Finally, we present an economic analysis to capture the reduction to plant capital expenditure that could be enabled by our mist-based system

# Chapter 1: Enhancing the injectability of high concentration drug formulations using coaxial lubrication

## 1.1 Introduction

In 2012, worldwide biopharmaceutical sales were estimated to reach US$163 billion, accounting for over 70% of the revenue from the top ten selling pharmaceutical products. [1,2] Monoclonal antibodies, enzymes, peptides and recombinant therapeutic proteins are all examples of biologic drugs that have transformed the pharmaceutical industry due to their high degree of specificity, potency, and efficacy compared to conventional small-molecule drugs.[3,4] Due to these benefits, over a thousand biologics targeting cancer, asthma, psoriasis, arthritic disease, and a wide range of infectious and non-infectious diseases are being developed. [5–7]

Currently, these drugs are predominantly administered in low concentrations (<30mg/ml) via intravenous injections at doses ranging from 5 to 700 milligrams. [8] Over the past few years, however, subcutaneous injection has emerged as an alternative delivery route as it *(i)* enables self-administration, *(ii)* reduces hospitalization and treatment costs, and *(iii)* increases patient compliance. [8] Unlike intravenous injections, subcutaneous injections require formulations that are far more concentrated (>100mg/ml) as injection volumes are limited to 1-1.5ml per dose. This constraint arises from high back pressures that can develop in subcutaneous tissue at larger volumes. [8,9] A non-linear relationship between formulation concentration and viscosity makes subcutaneous formulations very viscous (20-60 cP) and therefore harder to inject, as illustrated in figure 1a: a highly viscous fluid (dyed blue) spreads significantly less than a low viscosity fluid (dyed green), when injected in a sponge at the maximal force we could apply manually (around 50N). [10–13] Consequently, the applicable force sets a limit to the concentrations of current formulations, as shown in figure 1b. This figure reports the injection force (for a flow rate of 4ml/min through a 27G needle) as a function of concentration for four monoclonal antibody solutions of the IgG1 isotype that have been reported in literature. [10–13] This figure also highlights the fact that an extensive range of formulation concentrations require more than 50N to be injected – the average maximum force that can be applied in a pinching motion to a syringe for subcutaneous injections. [14–16]

While larger needle gauges or prolonged injection times through the use of syringe pumps could overcome challenges associated with the low injectability of high concentration formulations, these approaches would negate the benefits offered by subcutaneous delivery due to a larger degree of pain and the requirement of a hospital setting, respectively. [17]

Needle-free jet injectors have also been proposed as a potential pathway to enable the delivery of high viscosity formulations. However, splashback of the jet stream and blood from the injection site, combined with observations of fluids being sucked back into the injector, have been reported to contaminate the injector and subsequent doses during repeated use. [18–21] These issues, together with the high cost of such injectors, prohibit their use in the context of self-administration, especially in the developing world.

Another recent approach consists of using particle encapsulation to create microscale carriers that can deliver highly viscous biologics. [22] However, protein inactivation, density-based separation, needle clogging, and a higher degree of manufacturing complexity are critical problems that need to be addressed to make this approach viable. [18,23–25] The lack of a practical methodology to inject high viscosity formulations has not only limited the applicability of subcutaneous biologic formulations but also hinders the development of new formulations, forcing developers to design formulations with lower viscosities. Therefore, there remains a pressing need to achieve injectability through a simple and inexpensive technique with minimal additions to the pharmaceutical manufacturing process, and without risk of cross-contamination.

Here we propose such a technique to enhance the injectability of highly concentrated drug formulations using core annular flows. In such a flow, a low viscosity fluid coaxially lubricates the transport of immiscible viscous fluids through the needle (figure 1c). This not only reduces the hydrodynamic resistance in the needle but also reduces shear forces on the payload material (inner fluid). Core annular flows have been explored as a lubrication technique, to facilitate the transport of viscous oils through pipelines. [26–28] However, these flows are not widely used in practice for oil transport due the difficulty in maintaining stable, co-axial lubrication over large length scales. [29] In microfluidics, dripping to jetting transitions of co-flowing liquids are used in droplet generators and emulsifiers. [30–32] However, the diameter of medical needles ($\approx$ 200 µm) is neither in the macroscopic scale of oil pipelines nor in the microfluidic scale. Hence it is important to understand how to establish and sustain a core annular flow in such needles.

In the case of a concentric core annular flow, the Navier-Stokes equations combined with the lubrication approximation can be used to predict the attainable pressure reduction coefficient $\eta$, as a function of the viscosity ratio $\lambda = \mu_i/\mu_o$. While these formulations can exhibit non-Newtonian behavior (specifically shear thinning) at high shear rates, only Newtonian behavior is considered in this work. [16,33,34] This is because the shear-thinning of these formulations is not sufficient to make them injectable. [34] The subscript $i$ denotes quantities related to the inner (viscous) fluid, and the subscript $o$ denotes those related to the outer (lubricating) fluid. With no-slip boundary conditions at the wall of the needle,

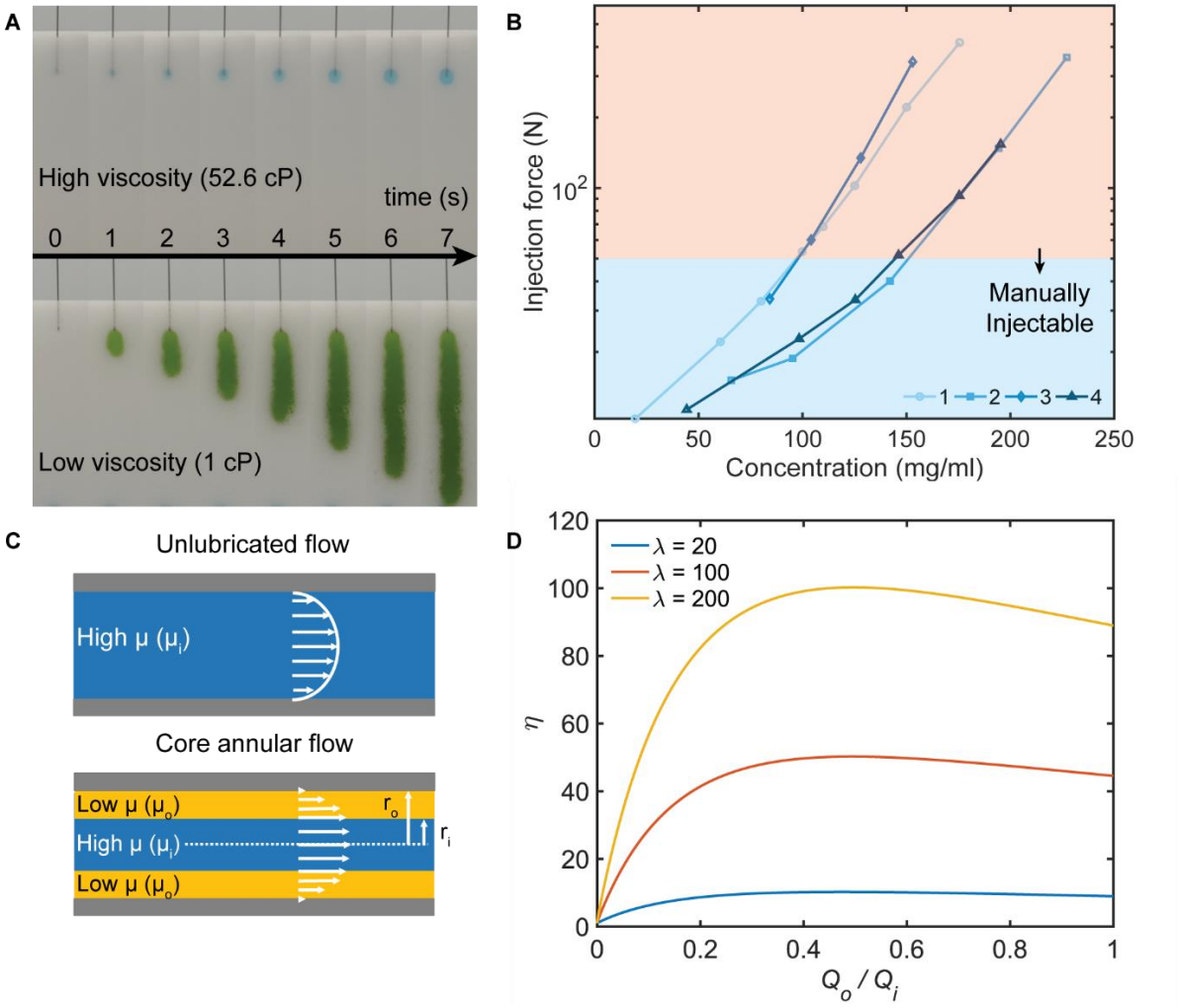


Figure 1: (a) Demonstrates the difficulty in the manual injection of a high viscosity solution (52cP glycerol/water, blue) compared to low viscosity solution (1cP water, green) through a 27G needle. The time-lapse image was taken over 7 seconds of manual injection into an absorbent sponge. The operator applied the maximum pinching force possible (approximately 50N) (b) The force required to manually inject four (labeled 1-4) highly concentrated monoclonal antibody solutions of the IgG1 isotype reported in literature exceeds the maximum force that is applicable in a pinching motion (50N). [10-16] (Forces calculated for a flow rate of 4ml/min) (c) Schematic cross-sections of unlubricated flow and core annular flow through a needle. (d) The pressure reduction coefficient ($\eta$) scales with the viscosity ratio ($\lambda$) between the formulation and the lubricant, demonstrating the promise of core annular flow as a methodology to make any formulation injectable

shear and velocity continuity at the interface of the two fluids, the pressure reduction factor can be expressed as (see Supporting Theory section for derivation):

$$\eta = \frac{\Delta P_{control}}{\Delta P_{Core\ annular\ flow}} = \frac{{r_i}^4}{{r_o}^4}\left(2\lambda\left(\frac{{r_o}^2}{{r_i}^2} - 1\right) + 1\right); \quad (1.1)$$

Plotting this pressure reduction coefficient as a function of the flow rate ratios (figure 1d) reveals that a maximum is reached when $Q_o/Q_i \approx 0.4$, followed by a slight decrease at high flow rate ratios. Pressure reductions up to 50x can be reached in theory, in the case of $\lambda = 100$, making core annular flows a promising candidate to reduce the force needed to inject viscous formulations manually significantly. The goal of our work is to develop a device that uses core annular flows to enable the injection of highly viscous formulations and to compare its performance to the expected pressure reduction from such flows. To achieve this, we first report the flow regimes observable in such a device and establish a regime map to indicate the flow rates and viscosity ratios at which core annular flow can be sustained in a needle. We then quantify the corresponding pressure reduction and compare our measurements with theoretical predictions. We design, fabricate, and test a first generation co-axial, double barreled prototype syringe to exhibit the capability of this technique to inject high concentration drug formulations.

## 1.2 Results and Discussion

### *1.2.1 Stability of core annular flows*

The setup shown in figure 2a was used to study the dynamics of core annular flows through a needle. Two syringe pumps were used to drive the inner viscous fluid and the outer lubricating fluid through a fluidic cross to establish the core annular flow. A digital pressure sensor (see methods) at the cross measured the pressure drop through the needle. A transparent needle was used to visualize the flow, and the dimensions of all components were chosen so that their hydrodynamic resistances are negligible compared to that of the needle (as shown in the supporting theory section). [35]

Due to the volume and dosing constraints of subcutaneous biologic injections mentioned earlier, volume fractions (of viscous payload) lower than 55% were not considered as it is undesirable to inject the same amount or more of the lubricant, than the drug formulation. In addition, figure 1d shows that the benefit of core annular flows is reduced at low viscous payload volume fractions ($Q_o/Q_i > 0.8$). Therefore, the flow rate of the inner viscous fluid was fixed at 1 ml/min, and the flow rate of the outer lubricant was varied from 0.1 to 0.8 ml/min. These values were chosen as they are in the range of flow rates required for a practical injection. [36] Figure 2b shows a map of the observed flow regimes for different flow rate and viscosity ratios. Two regimes occur in our phase space: a viscous displacement regime at low lubricant flow rates, and a core annular flow regime as the lubricant flow rate increases. In the viscous displacement regime, the viscous fluid first fills the entire cross-section of the needle, inducing both fluids to back-flow into the lubricant inlet. However, this back-flow cannot be sustained due to the constant mass flux imposed on the lubricant, resulting in a sudden overflow of the lubricant into the needle.

This flow decreases until being completely hindered once again, and the process repeats. This cyclic behavior is shown in the temporal diagram of a cross-section of the needle (Figure 2c): it leads to unsteady and significantly worse lubrication compared to the core annular flow regime (Figure 2d).

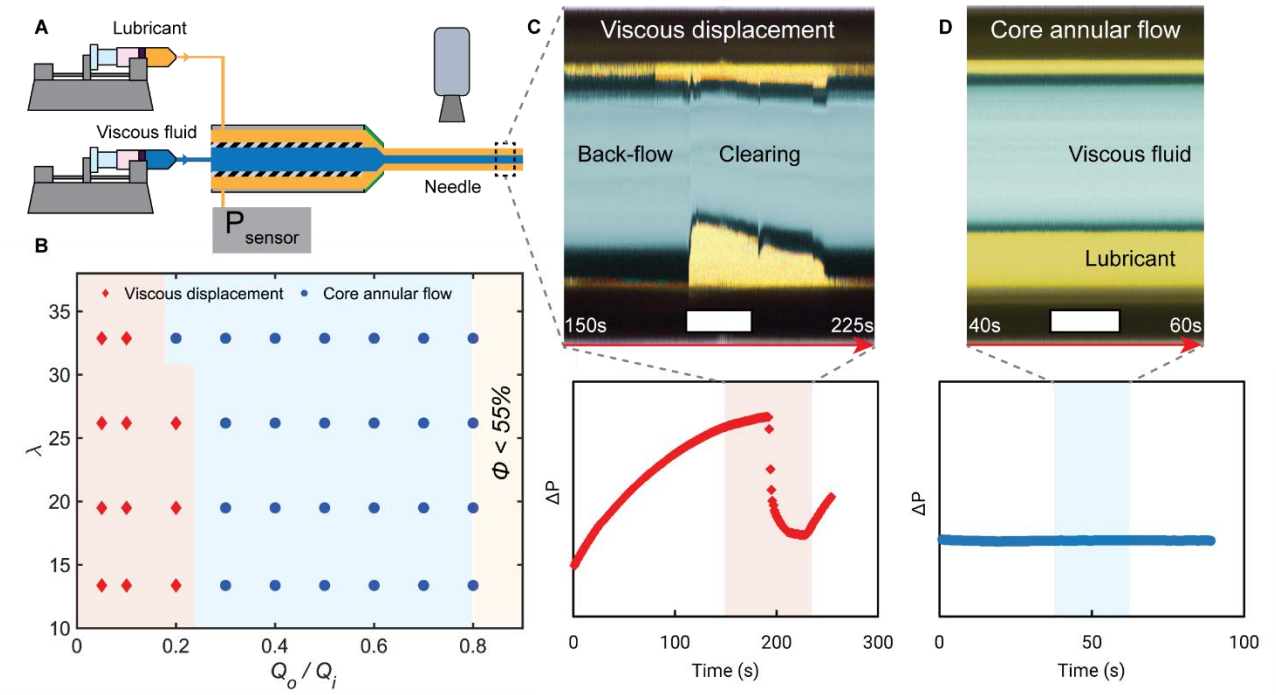


Figure 2: (a) Experimental setup used to study flow regimes and the lubrication effect of core annular flows. (b) Flow regimes observed in the needle for the chosen flow rates. Volume fractions below 55% were not experimentally explored as it is not of interest from a drug injectability perspective. (c) False-colored temporal diagram of a cross-section of the needle (needle inner diameter = 304.8 µm) combined with a pressure versus time plot, highlighting the viscous displacement regime. This regime involves cyclic switching between a primary state where the viscous fluid fills the entire cross-section of the needle to a second state where the two fluids flow as an intermittent core annular flow. This results in a high and unstable pressure drop in the needle. (d) The core annular flow regime, on the other hand, is stable over time and results in a much lower steady-state pressure drop, which is essential to enhance injectability. The scale bars are 100 µm wide.

*1.2.2 Experimental Pressure reduction*

Figure 3a reports the experimental pressure reduction coefficient (mean ± std. error) as a function of the ratio between the lubricant flow rate and the viscous fluid flow rate, for several viscosity ratios. Experiments corresponding to the viscous displacement regime ($Q_o/Q_i \leq 0.2$) exhibit larger errors due to the cyclic nature of this state. Thus, the average

pressure reduction factors in this regime are also much lower than in the case of the core annular flow regime ($Q_o/Q_i > 0.2$).

While the pressure reduction performance follows a similar trend as expected from concentric core annular flow theory, we observe a significant difference in the magnitude of the pressure reduction coefficients (predicted value for $\lambda = 20$ is $\eta \sim 10$ in concentric core annular flow while the experimental value for $\lambda = 19.5$ is $\eta \sim 4.5$). This lower performance originates from the eccentricity caused by the density difference between the two phases, as revealed in figure 3b (false-colored digital photograph of a side view of the needle demonstrating eccentricity due to buoyancy).

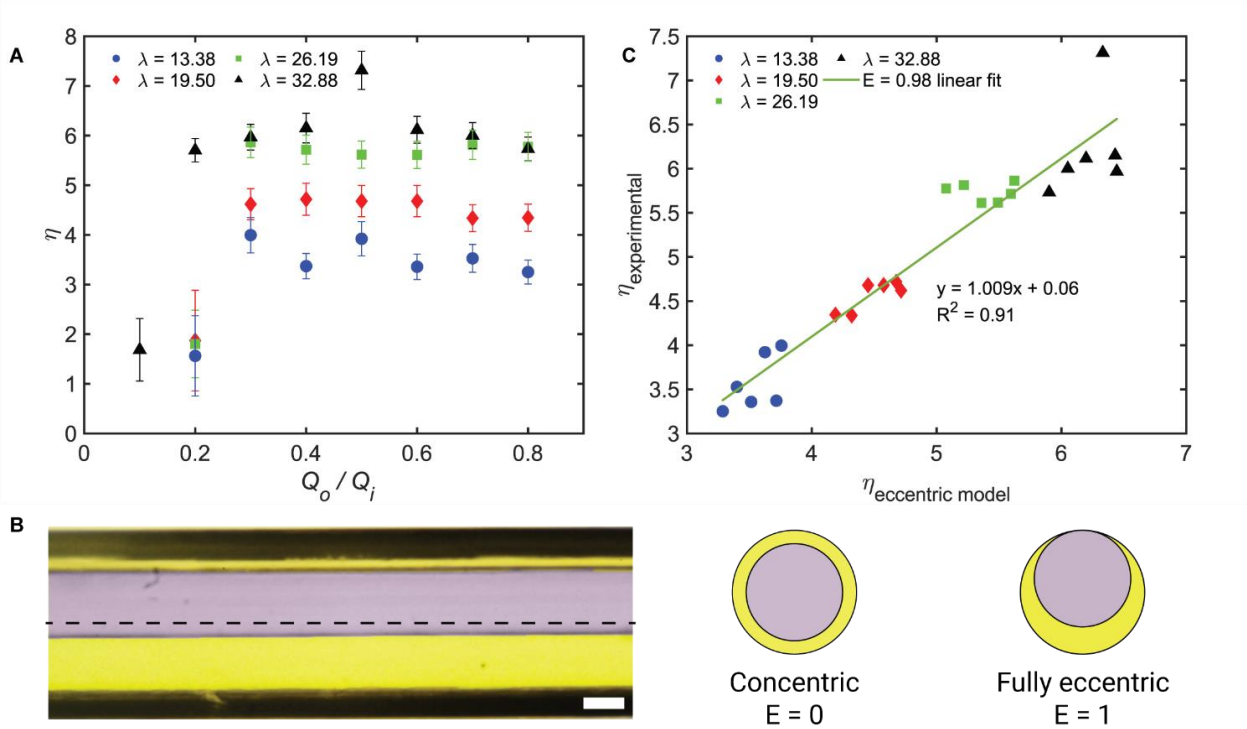


Figure 3: (a) Experimental results show that the pressure reduction coefficient follows a similar trend to concentric core annular flow theory. The pressure reduction coefficient ($\eta$) is plotted as a function of the ratio between the lubricant ($Q_o$) and viscous fluid ($Q_i$) flow rates for different viscosity ratios ($\lambda$). (b) The maximum pressure reduction coefficient is still lower than expected, compared to concentric flow theory for all the viscosity ratios and this reduced performance is attributed to the eccentricity of the viscous fluid due to the density difference between the two fluids. A false-colored digital photograph of the needle demonstrates this eccentricity (needle inner diameter = 304.8 µm, scale bar is 100 µm wide). (c) Illustrates that the performance limit is indeed well described by laminar eccentric core annular flow theory (E = 0.98 used for the eccentric model).

*1.2.3 Eccentric coaxial lubrication*

In order to account for the eccentricity, we solve the Navier-Stokes equations in a bipolar coordinate system, following the approach of Bentwich et al. [37,38] By doing so, we derive a modified expression for the pressure reduction coefficient (equations S18 – S21), featuring an eccentricity parameter $E$, which ranges from 0 (non-eccentric) to 1 (fully eccentric) (Figure 3b). Figure 3c shows excellent agreement between the experimental measurements for the pressure reduction coefficient and those derived from the eccentric core annular flow model using $E$=0.98, indicating that the model effectively captures the performance of core annular flows in realistic conditions (i.e., without density matching). The experimental results and the model reported here correspond to the base-line scenario where the syringe is kept horizontal. The pressure reduction achieved in the horizontal case represents the most conservative measure of the benefit offered by core annular flows. While a syringe placed perfectly vertical would not experience buoyancy induced eccentricity in the needle, any deviation from the vertical orientation rapidly leads to eccentricity. By considering the timescales of convection and eccentricity formation, we developed a model that can capture the influence of the syringe orientation and it is discussed in section 1.2.7.

*1.2.4 First generation prototype*

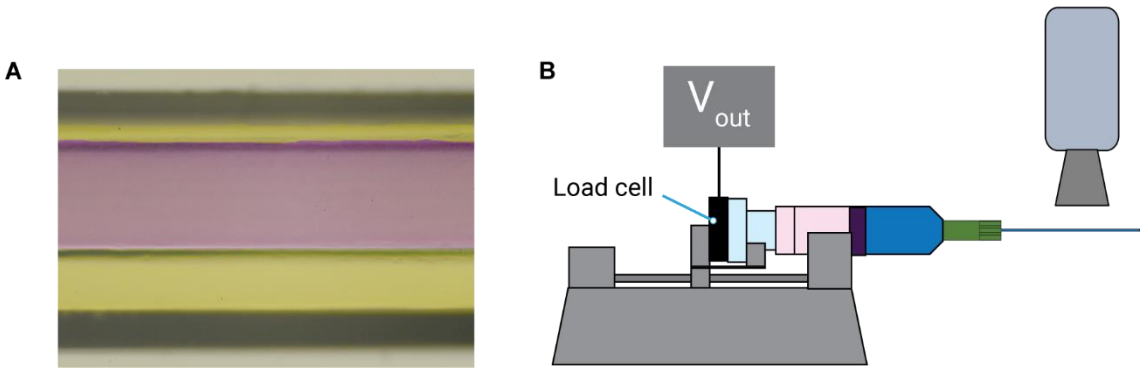


Figure 4: (a) False-colored image showing core annular flow in a needle connected to the double barreled syringe. (b) Experimental setup used to quantify the performance of the double barreled syringe.

We demonstrated that the discrepancy between measurements and theoretical predictions of the pressure reduction coefficient is due to the buoyancy induced eccentricity of the core annular flow. Even so, our experiments show that up to a 7x reduction in pressure (for $\lambda \approx 32.9$) remains achievable, indicating that the regime of injectable concentrations can be expanded significantly using core annular flows. Therefore, to implement this knowledge into a practical device, we designed and fabricated the double barreled syringe shown in figure 5a and figure 5b. It consists of an outer barrel that contains the lubricant and an inner barrel that holds the viscous payload. A six-milliliter syringe barrel from VitaNeedle® was used as the outer barrel. The fluids are driven by corresponding outer

and inner plungers with a movable outer gasket that ensures leak-proof operation. The dimensions of the barrels were chosen so that during the displacement of the plungers, the ratio of lubricant flow rate to viscous fluid flow rate is approximately 0.59, which is significantly above the threshold value of 0.2 required to sustain a core annular flow. The simplicity of this design makes it easy to manufacture, as it can be made using injection molding or blow-fill seal processes, ensuring similar ease-of-use and cost as current commercial medical syringes and needles. Figure 4a shows the core annular flow established in a needle connected to our double barrel syringe, indicating that it indeed operates in the core annular flow regime.

Visual evidence of the enhancement in manual injectability is shown in figure 5c, where we observe better liquid spreading in a sponge when a highly viscous fluid is injected using our double barreled syringe (dark blue) compared to a commercial syringe (light blue). In order to quantify this improvement, we compared the forces needed to inject a water-glycerin solution (26.3 cP) with our double-barreled syringe and a commercial syringe for the same volume flow rate. The injection force was quantified with a load cell (see Methods) mounted on a syringe pump (Figure 4b). The measured forces were used to calculate the force reduction coefficients, $\eta_{DBS}$ and $\eta_{needle}$ which are defined as shown in equation 1.2 and equation 1.3.

$$\eta_{DBS} = \frac{\mathrm{F_{commercial\ syringe}}}{\mathrm{F_{Double\ barreled\ syringe}}} \tag{1.2}$$

$$\eta_{needle} = \frac{\mathrm{F_{commercial\ syringe}} - \mathrm{F_{commercial\ syringe-without\ needle}}}{\mathrm{F_{Double\ barreled\ syringe}} - \mathrm{F_{Double\ barreled\ syringe-without\ needle}}} \tag{1.3}$$

Figure 5d shows the experimental force reduction coefficients obtained from our double barreled syringe. Both the commercial and double barreled syringe were run with and without the needle in order to quantify the resistance of the barrels. One has to mention that our proof-of-concept design suffers from significant friction between the barrels and the plungers, resulting in a low value for $\eta_{DBS}$. However, this friction can be largely eliminated by using existing syringe manufacturing techniques (such as injection molding to make more appropriately sized gaskets). Pluger break-loose and glide forces have largely been minimized using these techniques in conventional syringes as they lie in the range of 1-9N compared to the 50N manual injectability threshold. [39] The larger variability observed for the needle ($\eta_{DBS}$) is due to the error propagation operations carried out to isolate the resistance of the needle alone. when the contributions of the barrels are removed, we observe a force reduction coefficient of 5 in the needle. This value lies within the theoretical prediction of the eccentric model with the eccentricity parameter E = 0.98, therefore emphasizing that the partially eccentric model accurately captures the performance of the proof-of-concept double barreled syringe.

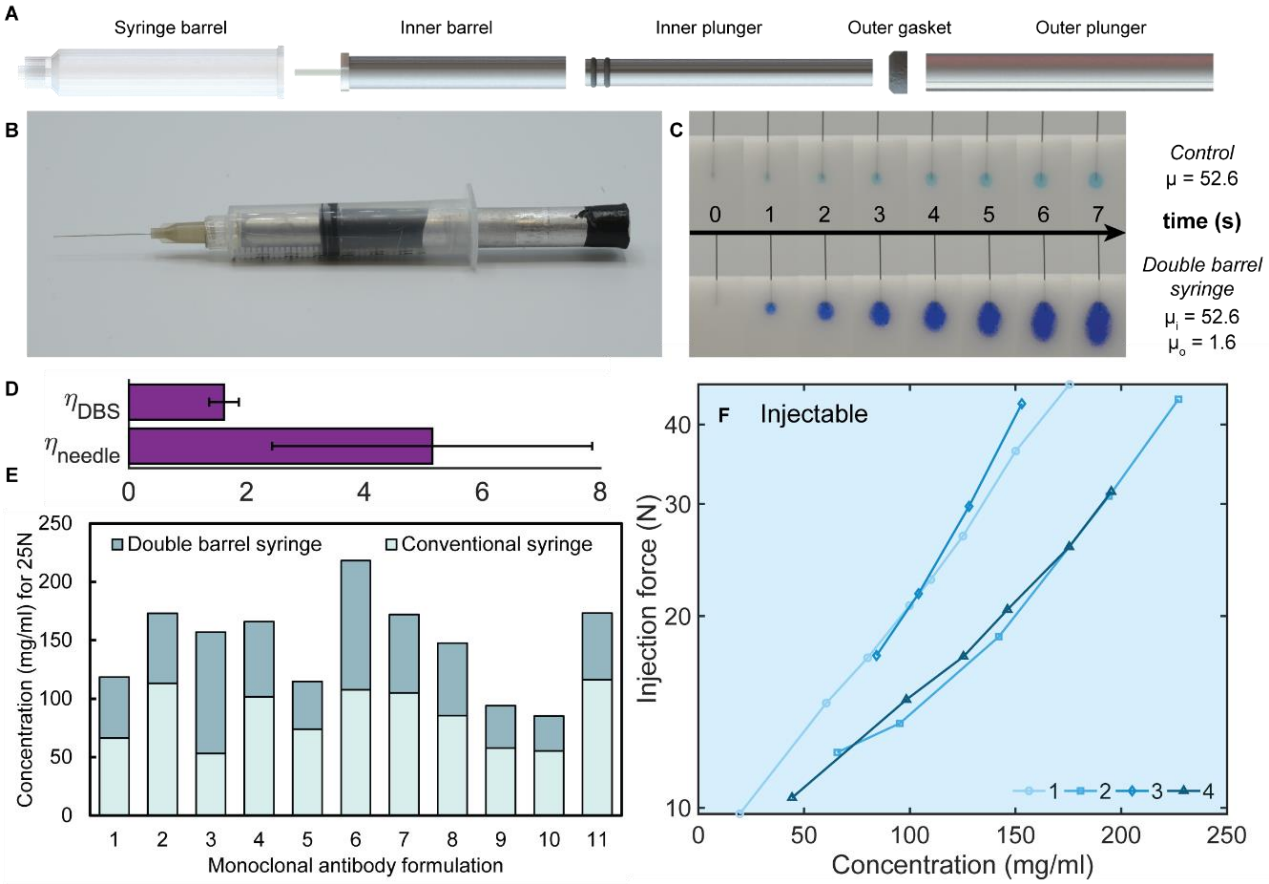


Figure 5: (a) Exploded view of the proof-of-concept double barreled syringe. (b) Photograph of the double barreled syringe (c)Time-lapse images comparing the injectability of a high viscosity formulation through a commercial syringe (light blue) and the double barreled syringe (dark blue). (d) Force reduction coefficient of the overall double barreled syringe ($\eta_{DBS}$) and the needle ($\eta_{needle}$) alone. (e) Demonstrates the increases in concentrations that are possible for eleven high concentration monoclonal antibody solutions of the IgG1 isotype reported in literature for a nominal injection force of 25N by using the double barreled syringe [10-13]. (f) Using E = 0.98, the predicted injection forces for four formulations from literature are calculated as a function of monoclonal antibody concentration. Compared to their corresponding values in commercial medical syringes (figure 1b), we show that the regime of injectable concentrations can be expanded significantly using core annular flows. [10–16]

The significant force reduction coefficient achieved here demonstrates the promise of the core annular flows to increase the threshold concentrations of biologic drugs that can be manually injected. Figure 5e indeed shows the increases in concentrations that are possible for eleven monoclonal antibody solutions reported in literature, while keeping injection force at a nominal 25N. It reveals that we can double (formulation 6) and even triple (formulation 3) the injectable concentration for specific monoclonal antibody formulations

using the double barreled syringe. [10–13] Furthermore, the reduction of force for lower concentration formulations could enable faster injections, or the use of smaller needles, resulting in less pain for patients . [17]

*1.2.5 The role of wettability in eccentric core annular flows*

A key feature to keep in mind in the design of the double barreled syringe is wettability. Indeed, if the inner fluid preferentially wets the interior needle surface, the outer lubricant flow might fail to coaxially lubricate the inner fluid, leading to an unstable core annular flow and, therefore, tremendous loss in the benefits of core annular flow. [32,40,41] This wetting criteria is why HFE-7500 was chosen as the model lubricant for this study, as HFE 7500 is more wetting towards the needle than the viscous aqueous payload. This is shown in figure 6, where HFE 7500 is observed to be thoroughly wetting on PTFE in the presence of glycerol (the viscous, model payload). This favorable wetting may be the reason why the flow is not wholly eccentric in our experiments (E = 0.98).

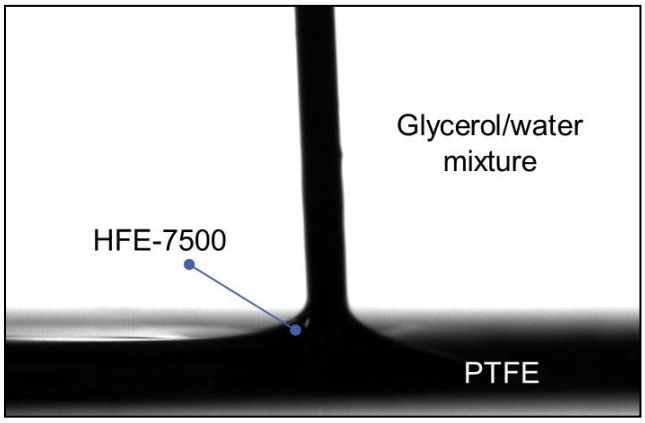


Figure 6: Contact angle measurement of HFE-7500 on a PTFE surface in an environment of a 26cP glycerol/water mixture.

*1.2.6 More robust lubricants*

Our proposal to use immiscible and biocompatible lubricants is motivated by a wealth of literature on immiscible vaccine and drug adjuvants. For example, squalene and other oil-based adjuvants have been used in thousands of patients at concentrations between (5-52%) (volume of immiscible oil/volume of aqueous components) in several types of injections, including subcutaneous injections without affecting drug formulation efficacy. [42–44] Here we used HFE-7500 as a model lubricant to demonstrate the pressure reduction benefits of core annular flows, but we understand that each drug formulation will have to be tested on our platform to identify the most appropriate lubricant-drug combination. The framework established here could also be used to explore aqueous and miscible lubricants. Figure 7 shows an example of water used as a lubricant and a mixture of glycerol and water used as the viscous inner fluid. While such miscible lubricants could allow for even safer injections into patients, buoyancy-based eccentricity could lead to

stratified flows rather than co-axial lubrication due to a lack of preferential wetting of the lubricant on the needle surface. A lower pressure reduction coefficient of $\eta \approx 2.6$ was measured for $Q_o/Q_i = 0.7$ and $\lambda \approx 26$ when water was used as a lubricant compared to $\eta \approx 6$ for the identical conditions with the preferentially-wetting HFE-7500. However, the design of the double barrel syringe can be optimized for water lubrication by balancing the different time scales (convection, eccentricity formation and mixing – defined below) to mitigate eccentricity and promote coaxial lubrication as discussed below. Such designs will be explored in later in this chapter.

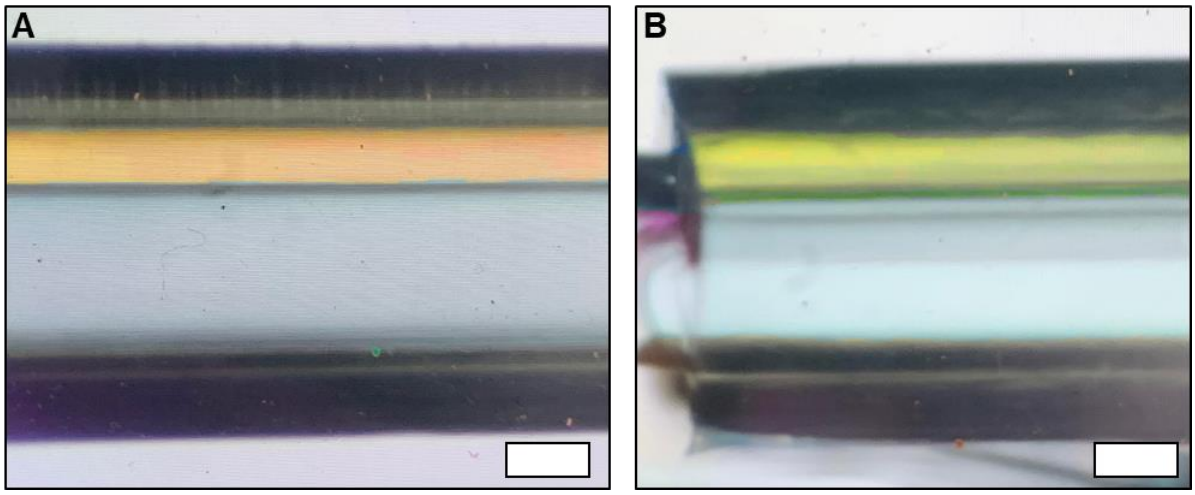


Figure 7: False-colored images of flow through a needle in which water is used as the lubricant at (a) the middle and (b) the exit of the needle. (needle inner diameter = 304.8 µm, scale bars are 100 µm wide).

Mixing is another phenomenon to keep in mind when miscible lubricants are used. The timescales of diffusive and convective transport can be compared using a Peclet number as shown in equation 1.4.

$$Pe = \frac{t_{diffusion}}{t_c} = \frac{l_d^2/D}{L/\bar{V}} \tag{1.4}$$

Here the characteristic length scale of diffsion $l_d$ is the inner diameter of a particular section of the system where the two fluids are in contact, $D$ is the diffusion coefficient, and tc is the convection timescale defined earlier. This ratio of these timescales in the hub and the needle for the glycerol – water system are 70 and 30, respectively (Coefficient of diffusion conservatively assumed to be $10^{-7}$).[45] This is consistent with the fact that in figure 7b, the two fluids are still well separated at the exit of the needle.

*1.2.7 Eccentricity timescales and the role of orientation*

Eccentricity formation in the double-barreled syringe is controlled by the timescale of convection ($t_c$) and the timescale of eccentricity formation ($t_e$). The timescale of convection is a measure of how quickly the inner fluid can convect through a particular section of length $L$ in the syringe-needle system, and it can be calculated, as shown in equation 1.5.

$$t_c = \frac{L}{\bar{V}} = \frac{LA_c}{Q_i} \tag{1.5}$$

Since it is preferred for the syringe to operate in the region of optimal concentric core annular flow wherever the two fluids are in contact, $A_c$ can be calculated as shown below.

$$r_i^* = \frac{r_o}{\sqrt{2 - \mu_o/\mu_i}};\ A_c = \pi(r_i^*)^2 \tag{1.6}$$

The expression for the optimal radius of the inner fluid ($r_i^*$) is derived by minimizing the pressure drop for a given inner fluid flow rate and fixed fluid properties (equation 1.6). The time scale of eccentricity formation is a measure of the time taken for an optimally concentric flow to become entirely eccentric in a given section of the system, and it can be calculated as shown in equation 1.7. Figures 8a and 8b show visual schematics that define the displacement length ($s$) and the orientation of the syringe ($\vartheta$).

$$t_e = \sqrt{\frac{2s}{\left|g\cos(\theta)\left(1 - \frac{\rho_o}{\rho_i}\right)\right|}} \tag{1.7}$$

Where $\varrho$ is used to indicate the densities of the two fluids, and $g$ is the gravitational constant. These timescales can be defined for regions of the system where the two fluids are in contact - the needle hub and the needle (cannula) itself. When $t_c/t_e < 1$ for a given section, the inner fluid convects through that section before eccentricity can form completely. Figure 8 shows how this timescale ratio varies in the hub and the needle as a function of the difference in density between the two fluids (Figure 8c-d) and as a function of the orientation of the syringe (Figure 8e-f). The dimensions of a 27G needle and a standard Luer hub were used in these estimations. For simplicity, only the cylindrical portion of the hub was considered and the constriction from the hub to the cannula is not considered. In addition, the effect of viscous drainage of the outer fluid is not considered for the estimation of the eccentricity formation timescale. Comparing the two timescales in the hub and the needle (cannula), suggests that eccentricity is established in the hub, which is consistent with experimental

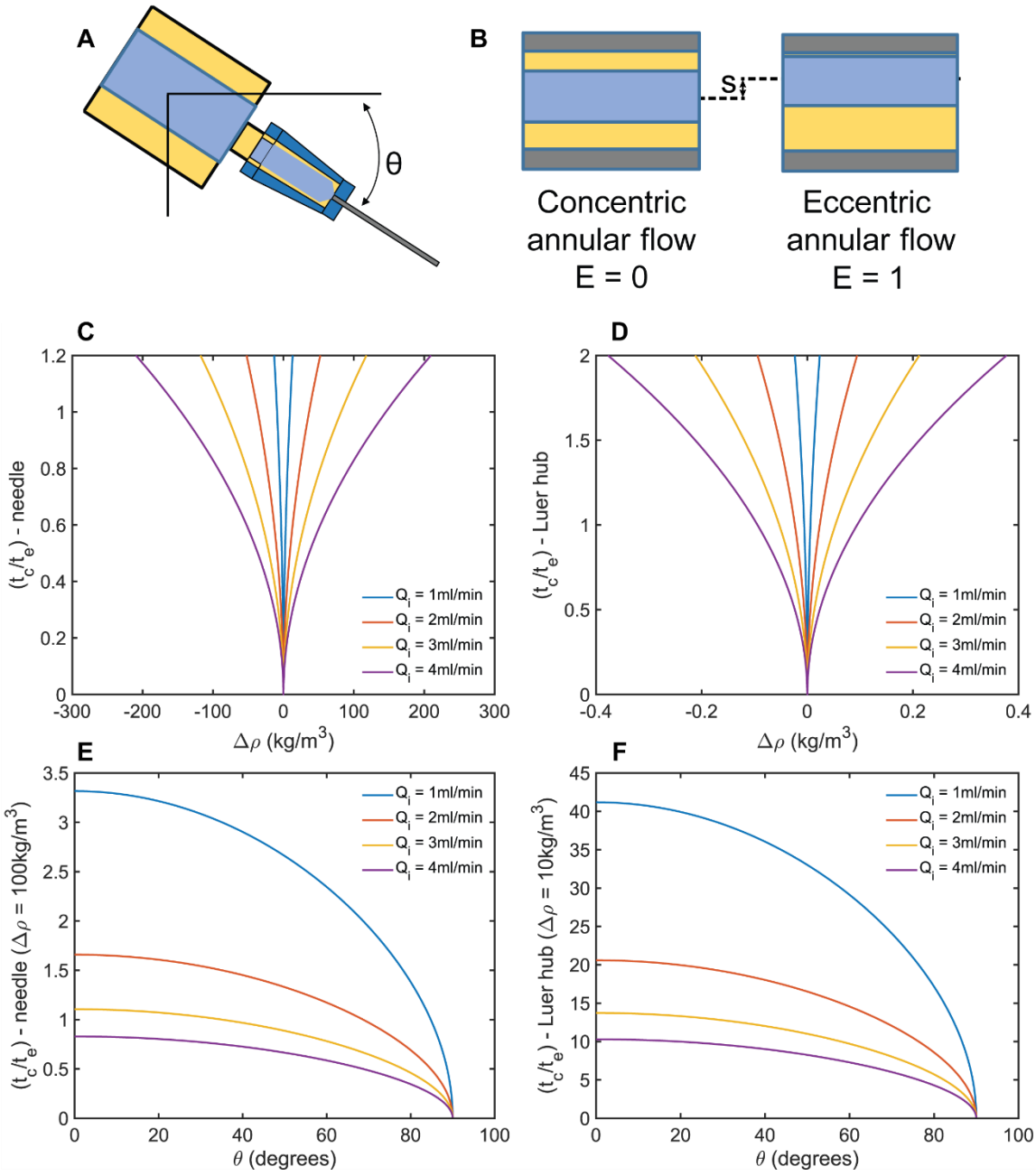


Figure 8: (a,b) Conceptual schematics of double barreled syringe indicating the orientation of the syringe ($\vartheta$) and the displacement length ($s$). $t_c/t_e$ is plotted as a function of the difference in density ($\Delta\varrho$) between the inner and outer fluids when the syringe is kept horizontal in the (c) needle and the (d) hub. $t_c/t_e$ is also plotted as a function of the syringe orientation in both the (e) needle and the (b) hub. $\Delta\varrho >= 400\text{kg/m}^3$ in all experiments where HFE-7500 was used as the lubricant.

observations. This is encouraging as a redesign of the hub could allow us to mitigate eccentricity formation in the system. In addition, Figure 8c suggests that eccentricity can be largely avoided in the needle if the flow enters the needle concentrically.

## 1.3 Conclusions and Outlook

The benefits observed in the core annular flow-based injection technique could be expanded to other subcutaneous delivery methods as well. Micro-needle patches, for example, could be made with smaller needles or could be used for shorter periods of time if the resistance to flow is reduced using core annular flows. This methodology also holds substantial promise for applications beyond biopharmaceuticals. For example, the lubricating effect of core annular flows could be used to inject other high viscosity or non-Newtonian fluids, such as bone putty or hydrogels. The reduced shear in such flows could also be applied to handle and dispense sensitive or primary cells where low shear is essential to prevent damage. [46–49]

In conclusion, we have demonstrated a simple, yet efficient technique to enhance the injectability of high concentration biopharmaceuticals using core annular flows. We established a regime map of flow rates and viscosity ratios required to attain stable core annular flow while minimizing the flow rate of the lubricant. We found that significant pressure reduction can be achieved in core annular flows for a variety of payload viscosities. We initially achieved up to a 7x reduction in pressure for a viscosity ratio of 33. In addition, we examined the role of buoyancy-induced eccentricity and compared our measurements to predicted pressure reduction in such eccentric core annular flows. We found that this model accurately captures the results of our experiments. We applied this knowledge to design, fabricate and test a first-generation prototype syringe. We showed substantial pressure reduction (up to 5x reduction for $\lambda = 26$) in our syringe which is consistent with our eccentric flow model, therefore significantly expanding the regime of injectable viscosities for biologics without increasing costs, risk of cross-contamination or manufacturing complexity by itself. We then examined the role of convection and eccentricity timescales in mitigating buoyancy effects and examined what would be necessary to achieve viscosity agnostic injectability.

## 1.4 Materials and Methods

### *1.4.1 Fluid preparation*

Mixtures of glycerol and water of different viscosities were used as the inner fluid in all experiments. HFE-7500 + 2wt% fluorosurfactant (obtained from RAN Biotechnologies) was used as the lubricant.

### *1.4.2 Rheology*

A TI ARG-2 rheometer was used to measure the viscosity of all the samples. A 40mm 2 ° cone geometry was used to measure the viscosity of all the glycerol solutions. Stepped flow tests were done where the shear rate was varied from $10s^{-1}$ to $500s^{-1}$. A 60mm plate geometry was used to measure the viscosity of HFE 7500. Here, the shear rate was varied from $1s^{-1}$ to $100s^{-1}$.

### *1.4.3 Contact angles*

Contact angle measurements were done using a Rame'-Hart contact angle goniometer.

### *1.4.4 Pressure reduction measurements*

Harvard apparatus PHD ULTRA™ syringe pumps were used to drive the fluids. A fluidic cross with 1/8" NPT female fittings was used to establish the core annular flow. Specifically, the high viscosity fluid flowedx through a (1/16" OD, 0.0575" ID) tube that traveled through the entire cross and a Luer adapter before entering the hub of the needle. The lubricant was brought through one of the branches in the cross and was allowed to exit to the needle coaxially with the inner viscous fluid. A 304.8 µm ID, 2" long PTFE needle was used in all experiments. The final branch of the cross housed a Honeywell ® 26PC series pressure sensor. The sensor is connected to a DC power supply and its output is measured using a Keithley ® 2450 sourcemeter operated as a voltmeter.

### *1.4.5 Testing the double barreled syringe*

An Omega engineering LC 307 series load cell was used to measure the force on the plunger. The load cell was attached to the driving plate of the syringe pump and a 3D printed adapter was used to ensure that the plungers made contact only with the load cell during operation. The sensor is once again connected to a DC power supply and its output is measured using a Keithley ® 2450 sourcemeter operated as a voltmeter.

# 1.5 Supporting Theory

*1.5.1 Concentric core annular flow model*

The assumption of laminar flow is valid as the typical Reynolds number for the viscosities, flow rates and diameters mentioned in the main text is below 20. The lubrication approximation is valid as typically, $Re_D \times D/L \approx 0.16$, where D and L are the diameter and length of the needle, respectively. The Navier Stokes equations in cylindrical coordinates therefore reduce to:

$$0 = -\frac{\partial P}{\partial z} + \frac{\mu_i}{r}\frac{\partial}{\partial r}\left(r\frac{\partial v_z}{\partial r}\right); \quad 0 \le r \le r_i \tag{S1}$$

$$0 = -\frac{\partial P}{\partial z} + \frac{\mu_o}{r}\frac{\partial}{\partial r}\left(r\frac{\partial v_z}{\partial r}\right); \quad r_i \le r \le r_o \tag{S2}$$

Where the subscript $i$ represents quantities related to the inner viscous fluid and the subscript $o$ denotes those related to the outer lubricating fluid. The boundary conditions of shear and velocity continuity at the interface of the two fluids, and the no slip condition at the inner wall of the needle can be used to calculate the flow rates of the two fluids in the case of core annular flow as shown in equations S3 and S4. (See figure 1c for definition of $r_i$ and $r_o$)

$$Q_{i,\,Core\ Annular\ Flow} = \frac{\pi {r_i}^4}{8}\frac{dP_{CAF}}{dz}\left(\frac{2}{\mu_o}\left(1 - \frac{{r_o}^2}{{r_i}^2}\right) - \frac{1}{\mu_i}\right) \tag{S3}$$

$$Q_{o,\,Core\ Annular\ Flow} = \frac{\pi}{8\mu_o}\frac{dP_{CAF}}{dz}((r_o^2 - r_i^2)^2) \tag{S4}$$

In the above equations, the pressure drop in the direction of the flow in both fluids is given by ($dP_{CAF}/dz$). This can be compared with the pressure drop required to flow the inner viscous fluid alone (in the case of an unlubricated flow). The Hagen – Poiseuille equation shown in equation S5 provides an expression for the inner fluid flow rate in this unlubricated case, where the pressure drop in the direction of flow is denoted by ($dP_P/dz$).

$$Q_{i,Poiseuille} = -\frac{\pi {r_o}^4}{8\mu_i}\frac{dP_P}{dz} \tag{S5}$$

The pressure reduction coefficient $\eta$ can be expressed as the ratio of the two pressure drops mentioned above when $Q_{i,Core\ Annular\ flow} = Q_{i,Poiseuille}$.

$$\eta = \frac{\Delta P_P}{\Delta P_{CAF}} = \frac{{r_i}^4}{{r_o}^4}\left(\frac{2\mu_i}{\mu_o}\left(\frac{{r_o}^2}{{r_i}^2} - 1\right) + 1\right) \tag{S6}$$

This coefficient captures the benefit of core annular flows in reducing the pressure drop across the needle compared to the unlubricated control.

*1.5.2 Estimating the hydrodynamic resistances in syringe-needle systems*

When considering a syringe and needle injection system, the total resistance to flow at a given rate can be modeled as three resistances in series: (i) the resistance in the syringe barrel/inlet (ii) the resistance from the constriction of the fluid as it moves from the inlet to the needle, and (iii) the resistance to fluid flow in the needle itself. Assuming that the plunger resistance is negligible compared to the resistance from the fluid flow, the pressure drop through this system can be estimated as shown in equation S7.

$$\Delta P_{total} = \Delta P_{inlet} + \Delta P_{needle} + \Delta P_{constriction} \tag{S7}$$

The first two terms on the right side of equation S7 can be modeled with the Hagen – Poiseuille equation. The pressure drop due to the constriction of the fluid from the inlet to the needle is modeled following the approach of Boger et al. [30]

$$\Delta P_{constriction} = 2L_{eq}\tau_{needlewall} \tag{S8}$$

Where $L_{eq}$ is a non-dimensional equivalent entrance length and $\tau_{needlewall}$ is the wall shear stress in the needle. Using this, equation S7 can be rewritten in terms of fluidic resistance:

$$\Delta P_{total} = Q \times R_{total};\ R_{total} = \frac{8\mu_i}{\pi}\left(\frac{L_{inlet}}{{r_{inlet}}^4} + \frac{L_{needle}}{{r_{needle}}^4} + \frac{L_{eq}}{{r_{needle}}^3}\right) \tag{S9}$$

Comparing the resistances involves estimating the magnitude of the three terms in parenthesis. For a 1ml syringe and a 27G needle, this leads to:

$$\frac{L_{inlet}}{{r_{inlet}}^4} = \frac{7.6 \times 10^{-2}}{(2.2 \times 10^{-3})^4};\frac{L_{needle}}{{r_{needle}}^4} = \frac{2.54 \times 10^{-2}}{(105 \times 10^{-6})^4};\frac{L_{eq}}{{r_{needle}}^3} = \frac{2}{(105 \times 10^{-6})^3} \tag{S10}$$

A conservative value of 2 is chosen for the equivalent entrance length ($L_{eq}$) based on prior studies in literature for a Reynolds number of 20. [30] Expressing the resistances in terms of their orders of magnitude reduces equation S9 to:

$$R_{total} = \frac{8\mu_i}{\pi}\left(O(10^{10}) + O(10^{14}) + O(10^{12})\right) \tag{S11}$$

This shows that the resistance due to the needle dominates the other terms. Equation S7 can, therefore, be reduced to:

$$\Delta P_{total} \approx \Delta P_{needle} \tag{S12}$$

*1.5.3 Smaller plunger diameter:*

While the approach presented in this work, tries to reduce the fluidic resistance in the needle, it is worth exploring how smaller plungers could be used to enhance injectability.

The force that has to be applied to the syringe plunger can be estimated, as shown in equation S13. Explicitly, the force of injection must overcome the friction force between the plunger and the barrel and the fluidic resistance to the flow through the needle.

$$F_{injection} = barrel\ friction + \frac{8\mu_i}{\pi}\left(\frac{L_{needle}}{{r_{needle}}^4}\right) Qi \times \pi r_{plunger}^2 \quad \text{(S13)}$$

While the inner diameter of the plunger can be reduced to achieve a reduction in the injection force, we can see that this approach has limitations. Considering the highest viscosity formulation presented in this work (56.25 cP), plunger radii would have to be reduced by a factor of 5.3x, 3x, and to achieve the force reductions offered by concentric and eccentric core annular flow respectively. This dramatically reduces the total syringe volume and the volume of the drug that can be injected. To inject the same volumes, these reductions in radii would require significantly longer barrels (28x and 9x longer respectively), and plunger displacement would also have to be correspondingly faster. These long barrels would be impossible to use manually, much harder to manufacture, and they would be more prone to breaking during operation. As discussed in the previous section, the hydrodunamic resistance to flow through the needle represents the fundamental bottleneck that needs to be addressed in syringe-needle systems.

*1.5.4 Eccentric core annular flow model*

The effect of eccentricity on the core annular flow was modeled using a bipolar coordinate system following the approach of Bentwich et al. [32, 33] Such a coordinate system allows us to derive an analytical estimate of the pressure reduction that can be achieved. This coordinate system ($\xi$, $\beta$) relies on two sets of non-concentric circles intersecting orthogonally, corresponding to constant $\xi$ and $\beta$ values, respectively. Therefore, in this system, the needle boundary, as well as the inner-outer fluid interface, can be represented by $\xi = \tau$ and $\xi = \sigma$. The Cartesian coordinates (non-dimensionalized in terms of the inner radius of the needle ($r_o$)) are related to the bipolar coordinates by the relation:

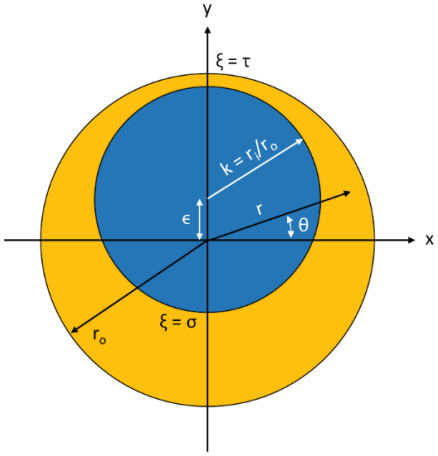


Figure 9: Schematic cross section of an eccentric core annular flow.

$$\xi + i\beta = \ln \frac{x + i(y - e^{\tau})}{x - i(e^{-\tau} - y)} \tag{S14}$$

The values of the constant $\tau, \sigma$ are given by:

$$\tau = \cosh^{-1} \frac{1 - k^2 - \epsilon^2}{2k\epsilon} \tag{S15}$$

$$\sigma = \cosh^{-1} \frac{1 - k^2 - \epsilon^2}{2\epsilon} \tag{S16}$$

Where, k is the ratio of the radius of the inner fluid interface to the needle's inner radius as shown in figure 10. $\epsilon$ is the eccentricity ratio, defined as the distance between needle's center and inner fluid's center expressed in terms of the inner radius of the needle. These transformations can be used to obtain the non-dimensional velocities $(v_j)$ of the core $(v_i)$ and the annular flow $(v_o)$ in the bipolar coordinate system defined as $v = \mu_o u / r_o^2 g_c \,.(-dP/dl)$. Finally, the dimensionless flow rates, (where $g_c$ is the gravitational constant) are obtained as:

$$q_j = \frac{8}{\pi} \iint v_j J d\xi d\beta \tag{S17}$$

Where $J$ is the Jacobian of the transformation matrix from the Cartesian to the bipolar coordinate system. On integrating, we get the final expressions as:

$$q_o = (1 - k^2)^2 + 2k^2\epsilon^2 - 8\left(1 - \frac{1}{\lambda}\right) k \sinh(\sigma - \tau) \sum_{m=1}^{\infty} \left[ \left\{ \tanh \overline{m(\sigma - \tau)} + \frac{1}{\lambda} \right\}^{-1} . \left\{ \frac{2(m\epsilon \sinh \tau - k^2)}{e^{2m\tau} + e^{2m\sigma}} + \frac{k^2}{e^{2m\sigma}} \right\} \right] \tag{S18}$$

$$q_i = \frac{1}{\lambda} k^2 (2 - k^2 - 2\epsilon^2) + 8\left(1 - \frac{1}{\lambda}\right) k^3 \sinh(\sigma - \tau) \times \left[ \frac{1}{2} + \frac{1}{\lambda} \sum_{m=1}^{\infty} \left\{ \tan \overline{m(\sigma - \tau)} + \frac{1}{\lambda} \right\}^{-1} e^{-2m\sigma} \right] \tag{S19}$$

Where $\lambda$ is the viscosity ratio of the inner fluid to the outer fluid as defined earlier and $m$ is a positive integer. The eccentricity parameter $E$ (equation S20) captures $\epsilon$ and $k$ into a single parameter that accounts for the degree of eccentricity.

$$E = \frac{\epsilon}{1 - k}; \tag{S20}$$

$E$ varies from 0 (concentric) to 1 (fully eccentric), as shown in Figure 3b. The pressure reduction coefficient $(\eta)$ is defined as the pressure drop across the needle in the eccentric core annular flow case compared to the unlubricated control, and is calculated as shown in equation S21.

$$\eta = \lambda q_i \tag{S21}$$

Using these definitions, we can plot the pressure reduction coefficient as a function of the eccentricity parameter $E$. By comparing the analytical solutions to our experimental data; we can find the best value of $E$ that fits the model with our experimental observations.

The best fit was obtained for $E = 0.98$ and the comparison of the model and our experimental results is shown in Figure 3c.

# Chapter 2: Reducing Pesticide Waste via Oil Cloaking

## 2.1 Introduction

Spraying is the most common method to deliver agrochemicals like pesticides to plants[50]. Poor spray retention is one of the most important inefficiencies in pesticide application. Sprayed droplets bounce or roll off of hydrophobic plant leaves causing a large majority of what is sprayed to find its way to the environment[51,52]. Pesticides are found in 90% of the time in agricultural streams, 50% in shallow wells and 33% in major deep aquifers across the USA[53]. A recent study has shown that 31% of all global agricultural soil is at high risk of pesticide pollution [54]. These excess pesticides not only affect soil chemistry but also cause the death of non-target organisms and damage soil microbiomes that are responsible for replenishing plant nutrients in the soil [55]. Once in the environment, pesticides have a catastrophic impact on public health. Unintentional and occupational exposure to pesticides causes around twenty thousand deaths and is linked to 385M annual cases of acute poisoning globally [56,57]. Pesticide pollution causes diseases like cancer, neurological conditions and birth defects and its impact is felt most in the developing world [56–60]. In addition to having a heavy global health and environmental cost, pesticides represent a major financial burden for farmers. Over $60B dollars of pesticides are used globally as they can contribute up to 30% of the production costs of crops like cotton [61]. Therefore, there is an urgent need to reduce pesticide waste and overuse and promoting spray retention offers a direct pathway to accomplish this.

The impact and bouncing of a liquid droplet on hydrophobic and superhydrophobic surfaces has been studied extensively [62–71]. In agricultural sprays, droplet sizes range from 50-600 µm and droplet impact velocities range from $1 - 8$m/s, which corresponds to a Weber number range of 1-600 [72–74]. During impact, such droplets undergo expansion driven by inertial forces and retraction that is driven by surface tension [71]. Whether the droplet sticks or bounces is determined by surface properties, such as surface energy and leaf micro-texture and droplet properties like surface tension, viscosity, density and impact velocity. Several works have proposed methods to increase droplet retention on plant surfaces. These methods include using (i) adjuvants to modify droplet properties such as surface tension, viscosity or density, (ii) additives that can disrupt the waxy coatings on leaf surfaces locally and promote adhesion, (iii) chemicals that generate microscopic pinning sites for droplets to stick or (iv) physical charged interactions to promote droplet adhesion.

Surfactants are the most widely used adjuvants that aim to enhance spray coverage and retention [75]. While their effect on improving the spreading of droplets on plant surfaces under static conditions is well documented, their ability to reduce the dynamic surface

tension of impacting droplets and suppress their rebound is more complex [76,77]. Recent work has shown that only specialized surfactants can diffuse to the droplet interface fast enough to reduce the dynamic surface tension of droplets during impact and arrest rebound [78,79]. In addition, surfactants suffer from a lack of universality as they must be chemically stable with a diverse range of pesticide chemistries. As they reduce surface tension, they also make the sprayed droplets smaller, which exacerbates pesticide drift and run-off [80,81]. Smaller droplets also tend to evaporate more quickly, which leads to product loss, especially for volatile pesticides [75]. Finally, some surfactants that are used in agriculture can be more environmentally and biologically toxic than the active ingredients in the pesticides. For example, the addition of ethoxylated amine surfactants to Roundup® make these formulations cause more mitochondrial damage and necrosis in human cells and much more toxic towards non-target organisms than the active ingredient – glyphosate alone [82–89].

Viscosity modifying adjuvants that utilize viscous dissipation during impact to prevent the droplets from bouncing off, offer limited improvement to spray retention efficiency on plant surfaces [90]. High molecular weight polymer-based adjuvants that can significantly enhance the extensional rheology of droplets have also been shown to slightly enhance spray retention (~2% enhancement on leaf surfaces). In addition to their moderate improvement, the need for the careful control of pH for such formulations presents a significant barrier to robust implementation for this method [91,92]. Electrostatic sprayers that physically charge spray droplets and introduce an attractive force towards grounded plant surfaces suffer from high costs that limit applicability [93,94]. Finally, prior work from our group has used polyelectrolytes to enhance droplet retention on plants [95]. In this approach, positively and negatively charged molecules are added to the sprayed liquid. The oppositely charged compounds undergo a precipitation reaction in-situ, creating microscopic pinning sites on an otherwise hydrophobic surface. While the approach has led to significant improvements in droplet retention both in the lab and in field trials, the need to keep the charged additives separated until they reach the plant surface requires a significant retrofit to the sprayers.

Unlike the above approaches which are either unsustainable, toxic, non-universal or expensive, plant-based oils hold great promise as adjuvants that can promote droplet retention [75]. Oils have been used in agriculture for centuries as they possess insecticidal and fungistatic properties [96,97]. Vegetable oils are generally recognized as safe and are understood to pose no risks to the environment and are widely used in food products and in agriculture [98–100]. Since they are readily degradable by microbes in the soil, these oils have a much lower environmental footprint than synthetic agrochemicals [101]. Their impact on crop health is well understood, and they are not phytotoxic when used correctly [96]. Some oils are more robust against resistance development in pests and some plant oils have minimal impact on non-target insects like honeybees [102,103].

As spray adjuvants, the lower surface energy of oils makes them stick more easily to hydrophobic leaves compared to water. Oils are predominantly formulated as oil-in-water emulsions, necessitating the use of surfactants – which have the drawbacks mentioned above – and the need for complex agitation methods at the point of use [75]. In comparison to oil-in-water emulsions, water-in-oil emulsions (>10% oil by volume) have been found to be more effective in enhancing retention. However the need for surfactants and the potential for phytotoxicity of such large oil contents limit the applicability of such formulations [104]. In this work, we propose a more universal approach that uses minute quantities of plant oils (<1% by volume) to enhance spray retention without the need for emulsification or surfactants. By cloaking the water droplets in plant oils, we can make compound drops that stick to hydrophobic plant surfaces as shown in figure 11. Compound drop impacts have received increased interest over the past few years [105–110]. However, water-in-oil compound droplet impacts have not been studied on superhydrophobic surfaces and at low concentrations of oil (≤1% vol.).

In Figure 11c-e, we show time-lapse images of water droplets sprayed using an agricultural sprayer onto a cabbage leaf for 3 seconds. The nozzle in this case produces droplets with a volume median diameter between 341-403 µm at velocities between 5-10m/s (see Methods). Some droplets pin wherever there are defects on the leaf but a majority of the sprayed water bounces off, highlighting the problem of poor droplet retention in conventional agrochemical spraying. (Supplementary Movie 1). In contrast, Figures 11f-h demonstrate the effectiveness of cloaking water drops with ~1% of soybean oil, a ubiquitous plant-based oil, which (i) is used in food products, (ii) is approved by the EPA for agricultural use, (iii) has minimal impact on the environment and (iv) is inexpensive [99,100,111]. With a third of the spraying time, we achieve more uniform coverage. We can quantify the ability of this approach to reduce pesticide waste by normalizing the spray time by the percentage of the leaf area covered with droplets. We find that oil-cloaking leads to a 5.25x reduction in pesticide waste, indicating the great promise of this simple, inexpensive and environmentally sustainable approach.

To fully understand this technique's potential to enhance droplet retention, we study it systematically with two types of nanoengineered superhydrophobic surfaces. These surfaces represent the most extreme case that agricultural sprays can encounter. Studying enhancements in droplet retention in this extreme case would provide a conservative benchmark for our methodology. We examine droplet impact dynamics at a variety of agriculturally relevant spray velocities and Weber numbers and systematically study the effect of cloaking with different oils of varying surface tension and viscosity. We explore the effect of oil fraction and present a simple energy state framework to explain the rebound suppression observed with oil cloaked droplets. Finally, we then test a practical embodiment of this system and demonstrate significant improvements in spray retention on nanoengineered superhydrophobic surfaces and vegetable crop leaves.

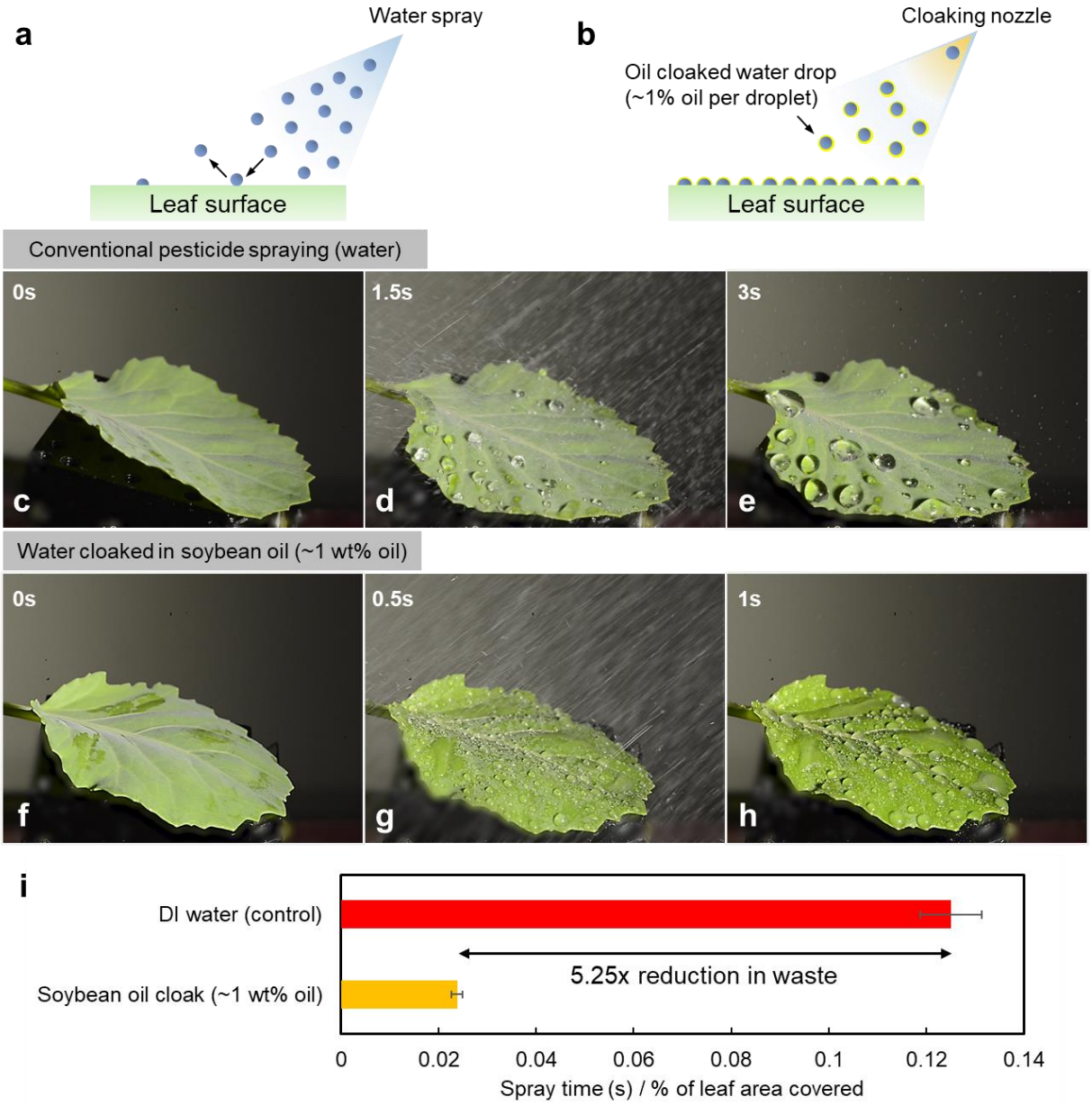


Figure 10: Oil cloaking leads to enhanced droplet retention on crops. Schematics of the experimental set-ups used to spray (a) water and (b) oil-cloaked water droplets onto leaves. Unlike conventional water sprays which bounce off of hydrophobic leaf surfaces, droplets that are cloaked in minute quantities of a plant-derived oil (ex: soybean oil $\leq 1\%$) stick to leaves uniformly. (c-e) Time-lapse images of water sprayed using a commercial agricultural sprayer onto a cabbage leaf for 3 seconds. Some droplets pin and accumulate but a majority of what is sprayed bounces off of the leaf (see Supplementary Movie 1). (f-h) Time-lapse images of water drops cloaked with soybean oil ( ~1 wt% oil) sprayed onto a cabbage leaf for 1 second. (i) Droplet coverage expressed as a percentage of total

leaf area and normalized by spray time for the two cases shows that oil-cloaking can lead to a ~ 5.25x reduction in over-spraying.

## 2.2 Results and discussion

*2.1.1 Single droplet impact setup and initial experiments*

Single water droplets of different diameters were created by forcing liquids through needles of different gauges. The oil cloaks were applied using a secondary needle as shown in figure 12. The flow rates of all fluids were controlled using syringe pumps. For oil fractions $<$ 1% by volume, the stainless-steel needles were hydrophobized (see Methods) to prevent any wicking losses. The impact velocities were changed by controlling the release height of the dispensed droplets. Silicon nanograss surfaces were used as model superhydrophobic surfaces in this work. The surfaces had an average texture size and spacing of around 200nm and they were functionalized with different hydrophobic modifiers (see Methods). The advancing and receding contact angles of DI water on this substrate were 163.9° and 159.3° respectively on the octadecyltrichlorosilane (OTS) coated surfaces and 166.6° and 164.8° on the trichloro(1h,1h,2h,2h-perfluorooctyl)silane (FS) coated surfaces respectively. The impact experiments were observed using a Photron Fastcam SA1.1 high speed camera.

Figure 12a shows time-lapse images of a water droplet (diameter $\approx$ 3 mm and impact speed $\approx$ 1.25 m/s) impacting on an OTS-Nanograss surface from the side and top-down views. The droplet behaves as expected, going through a symmetric retraction phase and completely rebounding from the surface (Supplementary videos 3,4). Figure 12b shows impacts under identical conditions (velocity and diameter) with droplets that are cloaked in 1% soybean oil by volume. While the expansion phase is nearly identical in terms of the maximum diameter and the expansion time, the retraction phase in the cloaked case is markedly different. (Supplementary videos 5,6). During retraction, the droplet's contact line is pinned to the surface due to the oil. This significantly reduces the retraction speed and causes the droplet to stick to the surface. Our setup allows us to track the maximum height of the droplet's center of mass ($h_{cm}$), offering a quantitative measurement to track rebound suppression. Illustratively, $h_{cm}$ is labeled in figure 12b. To confirm that the spreading phase of the impacts are undisturbed, and to study the dynamics of rebound suppression more thoroughly, we conducted drop impact experiments with 9 different oils of varying viscosities and surface tensions.

*2.1.2 Impact dynamics*

Figure 13a shows the time evolution of the contact diameter of droplets ($D(t)$) normalized by their initial diameter $D_0$ for 6 representative oil cloaking conditions. These experiments were all conducted at 1% oil fraction by volume and at an impact velocity of $\approx$1.25 m/s on OTS-coated nanograss surfaces. Only the control DI water droplet loses contact with the surface after rebound under these conditions as all the oil cloaks were successful in

suppressing rebound. The observations in figure 12 are further confirmed here, as the expansion phase is approximately identical in terms of maximum droplet diameter and the expansion time for all the droplets. During the retraction phase the contact lines of

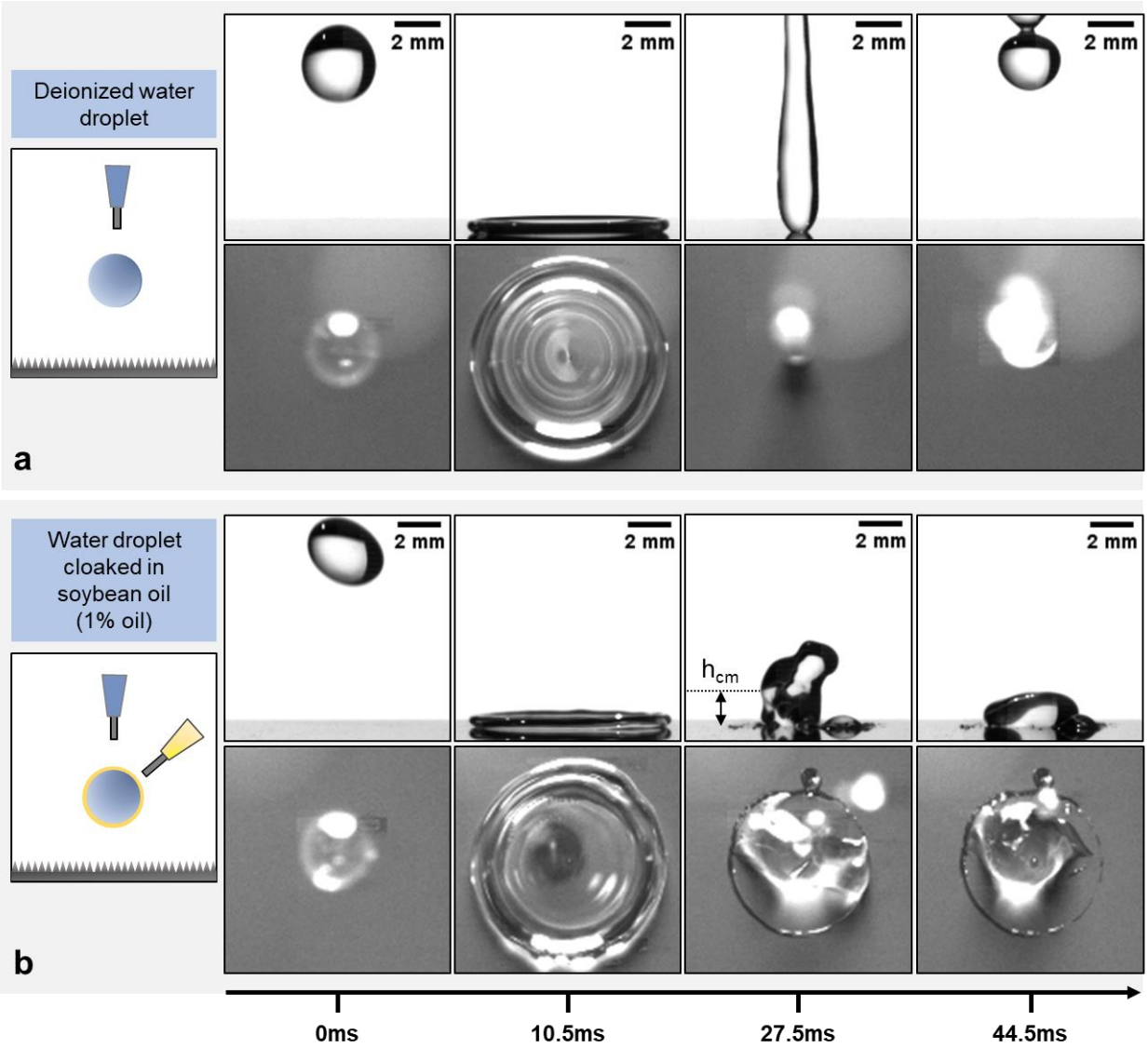


Figure 11: Single droplet impact on an engineered superhydrophobic surface. Schematics of the experimental setups used to study droplet impact are shown in the left column. Time-lapse images of impacts of (a) a water droplet and (b) a water droplet cloaked with soybean oil (1% oil by volume) from side and top-down views. The DI water droplet undergoes a symmetric retraction phase and maintains a high contact angle with the surface until eventually bouncing off (see Supplementary Movies 3, 4). The oil cloaked droplet undergoes a nearly identical expansion phase, however, the droplet pins during retraction and experiences a significant reduction in its receding contact angle. This pinning leads to the suppression of the rebound and leaves the droplet adhered to the

surface and constrains the maximum rebound height of the center of mass ($h_{cm}$) (see Supplementary Movies 5, 6).

the cloaked droplets begin to pin to the surface and slow down the receding front. Figure 13b shows the normalized maximum diameter for impact experiments with different oil cloaks, droplet sizes and impact velocities. The Weber numbers of the droplets were varied from 45-639 and the Reynolds numbers from 1972 – 7875 to span agriculturally relevant conditions. For this regime, the normalized maximum diameter at full expansion scales as shown in the equation below.

$$D_{max}/D_0 = f(Re, We) = \frac{We^{1/2}}{1.24 + We^{1/2}Re^{-1/5}}$$

where We is the Weber number and Re is the Reynolds number, as was shown in previous studies for droplet impact on superhydrophobic surfaces [112]. Once again, we observe that the maximum diameters are nearly identical for cases with and without oil cloaks and follow the trend indicated by equation 1. This demonstrates that the expansion phase of the droplet impacts is largely unaffected by the presence of an oil cloak at a variety of impact velocities and for different oils.

*2.1.3 Rebound suppression*

Focusing our attention now on the retraction phase and the rebound behavior of cloaked droplets, we revisit the maximum height the droplet's center of mass - $h_{cm}$ as defined earlier. Using the highspeed videos of the droplet impacts, we measure $h_{cm}$ of the droplets and normalize it by the initial droplet diameter $D_0$. (See Methods for the estimation of center of mass). Figure 13c plots the normalized rebound height for various impact velocities, oil cloaking conditions and surfaces. In all of these experiments, the oil fraction was kept constant at 1% by volume for the cloaked droplets. This plot demonstrates the robustness of the approach in promoting droplet retention. Regardless of the type of the oil, the oil viscosity or oil surface tension, all the cases with cloaking led to droplets sticking on superhydrophobic surfaces for velocities from 0.8 – 2.3 m/s which correspond to the agriculturally relevant We numbers of 81-646). Oil viscosities were varied between 1.3cst and 68cst, as any oil that is too viscous would be difficult to work with in practice. The surface tensions of the oil were varied as much as possible, between 16mN/m to 32mN/m.

We observe a general trend of lower $h_{cm}$ for higher surface tensions and viscosities in these experiments. At the higher end of the impact velocities we explored, we observe splashing of both the DI water droplets and the oil cloaked droplets. Interestingly while the satellite droplets in the control case scatter off the surface, nearly all the satellite droplets in the oil-cloaked case adhere to the surface (see Supplementary movies 7,8). Typically, smaller droplet sizes that are more prone to drift are chosen to enhance coverage on plant surfaces, but these results indicate that our methodology could enable the use of large droplets that

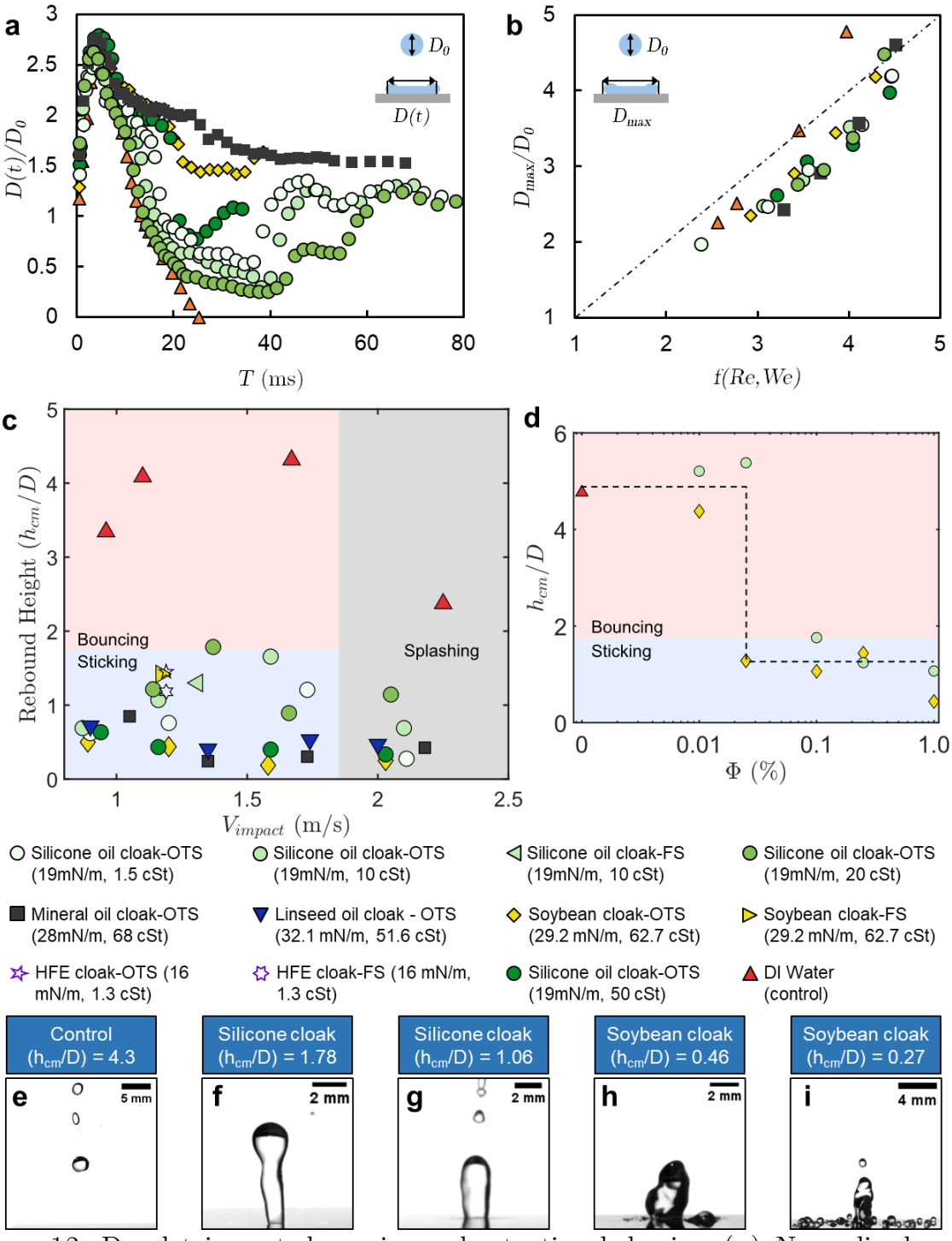


Figure 12: Droplet impact dynamics and retention behavior. (a) Normalized contact diameter as a function of time for 7 different oil cloaks for an impact velocity $\approx 1.25$m/s. Complete rebound is only observed for the pure water drop as contact is always maintained for all the oil-cloaked droplets (1% oil by volume). (b) Normalized maximum diameter as a function of the correlation function $f$ (We,Re). The weber number spanned 45 – 639 in our experiments. (c) Rebound height of the center of mass of droplets ($h_{cm}$)

is normalized by droplet diameter ($D$) for different impact velocities, oils and oil viscosities. All oil cloaked droplets had an oil fraction of 1% by volume and diameters ≈ 3mm. The bouncing transition is defined at h/D = 1.75, where the droplet lifts off the surface completely. All the oils helped suppress droplet rebound at a variety of impact velocities. (d) Rebound height of the center of mass of droplets ($h_{cm}$) normalized by droplet diameter ($D$) for different impact experiments is plotted as a function of oil volume fraction in cloaked droplets. 10cSt silicone oil and soybean oil were chosen as representative oils and both demonstrate the robustness of rebound suppression even for droplets with 0.1% of oil by volume (see Supplementary movies 9-13). (e-i) Snapshots of the highest points of the centers of mass of droplets during retraction or rebound for selected experiments. The labels for these snapshots indicate the oils used, the normalized rebound heights.

are resistant to drift while still benefiting from enhanced coverage afforded by satellite droplets.

*2.1.4 Effect of oil volume fraction*

Figure 13d demonstrates the effect of the oil fraction for two representative oils of low and high viscosity. Both oils are effective at preventing retention at 0.1% by volume, furthering the practical robustness of our approach. This volume of oil is comparable to the total amount of adjuvants currently used in agricultural spraying, including when oil-in-water emulsions are employed [75].

Supplementary videos 9-13 and supplementary figure 1 indicate some of the complexities that arise at lower oil fractions. As the volume fraction reaches 0.1%, we notice that the rim of oil that pins the droplet becomes discontinuous. This rim subsequently disappears as the oil fractions go below 0.1%. At these volume fractions, the average contact angle during the retraction phase also changes drastically from about 30° to about 140°. At 0.01% volume fraction, the retraction phase is comparable to that of a DI water droplet, indicating that there is a minimum amount of oil needed for the approach to be effective. Figures 13e-i show some examples of the maximum normalized rebound height for different impact conditions to highlight the distinction between the bouncing, sticking and splashing regimes.

*2.1.5 Energy dissipation in cloaked droplets*

We have been able to demonstrate that oil-cloaking offers a simple yet robust approach to enhance droplet retention on superhydrophobic surfaces over a range of agriculturally relevant impact conditions, for a wide range of oils, oil viscosities and oil volume fractions. However, it's also clear from the top-down videos of these impacts (Supplementary video 6, 9-13) that the mechanisms that govern retraction dynamics are fairly complex. There are several macroscopic and microscopic pinning events that lead to energy loss during retraction. These videos indicate the formation of a rim of oil plays a role in pinning the

droplets to the surface. However, it is also evident that the thickness, continuity and symmetry of the rims are highly variable. While some prior work has been done on the formation of compound droplet rims experimentally and in computational studies, this particular behavior hasn't yet been observed [107,108,110]. An added complication arises when the volume fraction of the oil goes down below 0.1%. In this case, oil scarcity at the interface needs to be considered in any model that attempts to accurately capture the dynamics of these compound droplet impacts. While explaining the explicit dynamics of this system will require more examination of the fluidic and interfacial interactions at play, we can use a simple analysis of energy states to explain droplet retention – which is the fundamental experimental outcome we care most about.

We can consider an impacting droplet in two states: (i) at the maximum diameter during impact and (ii) after the droplet has rebounded. We first focus on the latter state. When a water droplet rebounds off of a superhydrophobic surface, its kinetic energy can be expressed as a product of its incoming kinetic energy and the coefficient of restitution ($e_0$) and shown in figure 14a. In the case of water droplets, the coefficient of restitution on a superhydrophobic surface is a function of the Weber number [113]. Using this trend, for any water droplet of a given size and incoming velocity, one can estimate the rebound kinetic energy that the droplet would carry. For any technique to suppress this rebound, this energy would have to be removed from the droplet. Returning to the other state of interest– when the droplet reaches its maximum diameter, we can consider two types of energy dissipation mechanisms as shown in figure 14a, one due to surface tension and another due to viscosity.

The work of adhesion ($E_s$) – the term that captures the amount of work needed to remove a droplet from a surface can be written in terms of the surface tension of the fluid in contact with the surface ($\sigma_{outer}$), the receding contact angle of the droplet ($\vartheta_r$) and the maximum radius of the droplet on the surface ($R_{max}$) as shown in the equation below [114].

$$E_s \sim \sigma_o(1 + \cos(\theta_r))\pi R_{max}^2$$

In the cloaked cases, we can assume that the entire contact area with the surface is covered by oil during the impact event. This is a reasonable assumption given the fact that the oil is preferentially wetting on the surface compared to water. We also choose to model dissipation in experiments where the oil fraction was 1 %; as at lower volume fractions, the situation is more complex due to the discontinuity of the oil ridge during the impact event. The second dissipation mechanism is only present in the oil cloaked cases and is due to the viscosity of the oil cloak itself. Using prior work on the viscous dissipation rate due to the oil cloak on droplets, we can express the viscous dissipation rate $E_{\mu}{}'$ as a sum of three terms, dissipation in the oil cap ($E\mu_I{}'$), dissipation in the oil film underneath the droplet ($E\mu_{II}{}'$) and dissipation in the oil ridge ($E\mu_{III}{}'$), as shown in the following equation set[115].

$$E_{\mu}{}' \sim E\mu_I{}' + E\mu_{II}{}' + E\mu_{III}{}'$$

$$E_\mu{}' \sim \mu_w U_r^2 R_{max} + \frac{\mu_w^2}{\mu_o} U_r^2 t + \mu_o U_r^2 R_{max}$$
$$E_\mu{}' \sim \mu_o U_r^2 R_{max}$$
$$E_\mu \sim \mu_o U_r^2 R_{max} t_{ret}$$

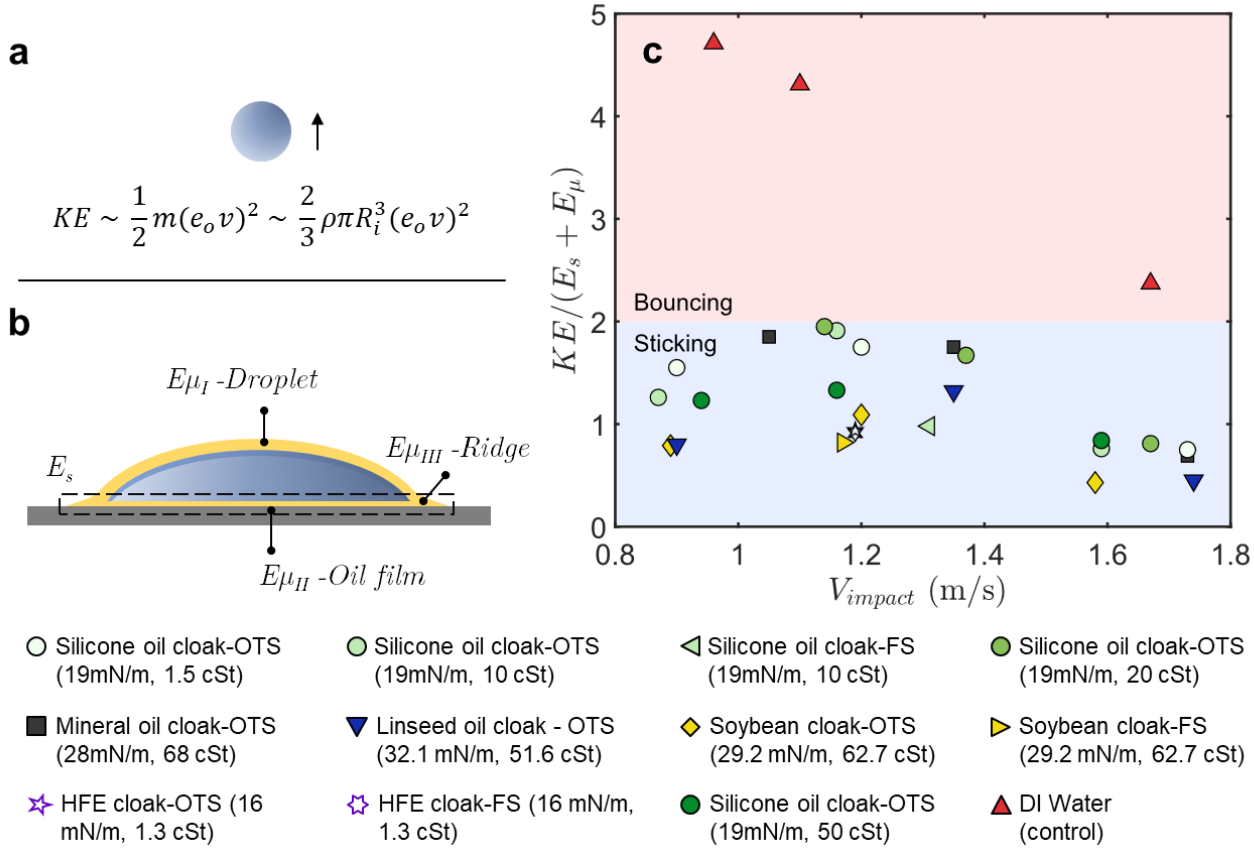


Figure 13: Sticking-bouncing transition for droplet impacts (a) As a pure water droplet rebounds from a superhydrophobic surface – the upward arrow indicating its motion away from the surface, it carries a kinetic energy that can be expressed in terms of the coefficient of restitution ($e_0$), the rebound velocity ($v$) and the mass of the droplet ($m$). (b) To arrest the rebound of such a droplet and make it stick to a surface, this kinetic energy must be removed from the droplet by the work of adhesion ($E_s$) and viscous dissipation ($E\mu_I + E\mu_{II} + E\mu_{III}$). (c) The data points correspond to droplet impacts at different droplet velocities, and oil cloaks. The shaded regions correspond to the different experimental outcomes. The vertical axis plots a ratio of the kinetic energy of rebound of a pure water droplet for all the experimental conditions (a particular impact velocity and drop size) and sum of the work of adhesion and the viscous dissipation. This demonstrates that in the case of oil-cloaking, the work of adhesion and the viscous dissipation is comparable to the rebound kinetic energy which leads to sticking.

In the equations above, $\mu_w$ and $\mu_o$ represent the viscosities of the water and oil, respectively. $U_r$ represents the velocity of the retracting droplet, $t$ is the thickness of the oil film underneath the droplet, $R_{max}$ is the maximum contact radius of the droplet in its fully expanded state and $t_{ret}$ is the retraction time for the droplet to go from its maximum diameter to its final contact diameter.
Comparing the relative magnitude of these terms, we can see that the viscous dissipation in the oil ridge at the contact line of the receding droplet would be the dominant term. We note here that the dissipation in the water drop doesn't need to be considered in this energy balance as it is already accounted for in the coefficient of restitution. Using this framework if the sum of the work of adhesion and the viscous dissipation scales with the rebound kinetic energy, the droplet will stick, and if the rebound kinetic energy is much greater than the sum of these terms, the droplet should bounce [71,116].

Figure 14b plots the rebound kinetic energy normalized by the sum of the work of adhesion and the viscous dissipation for each experimental condition that our model is applicable to. We explicitly do not plot data points that fall in the splashing regime as our estimate of the coefficient of restitution does not apply to those data points. We also do not consider oil volume fractions <1% given that the oil might not cover the entire interfacial area in those cases. For each droplet, we estimate the rebound kinetic energy that would be carried by a water droplet of similar size and incoming velocity using the coefficient of restitution. We estimate the work of adhesion and the viscous dissipation using the maximum contact diameter observed during each droplet impact. The contact angle used in this case is the quasi-static receding angle of the compound droplets on the superhydrophobic surface as reported in Supplementary Figure 2. Given these clarifications, we can see that the sum of the work of adhesion and viscous dissipation, scales well with the rebound kinetic energy for all the oil cloaked droplets, illustrating why they are able to stick. In contrast, the pure water droplets (which are the only experiments in which the droplet rebounded) have kinetic energies that are approximately 3x larger than the sum of the dissipative terms.

*2.1.6 Cloaking timescales*

Given that our energy dissipation model is able to capture the rebound behavior of droplets accurately, it's worth commenting on higher viscosities and the effect of the cloaking timescale. Supplementary movie 14 shows the impact of a droplet cloaked in 500 cSt silicone oil with a 1% oil volume fraction. While this high viscosity oil slightly effects the retraction phase, as compared to the pure water case, it is much less effective at suppressing rebound than the other cases of cloaked droplets where the oil viscosity was less than 70 cSt. This experiment with extremely a high viscosity oil thus provides some insight into cloaking timescales and its importance in rebound suppression. Indeed, the simple energy state model presented above would have predicted that the droplet would stick provided all other assumptions held. However, prior work on cloaking timescales of

oils of different viscosities on water drops suggest that the assumption of the oil covering the entire interfacial area wouldn't hold in this case of cloaking with a highly viscous oil [117,118]. Specifically, all of the other oils that were used in the study have viscosities $< 70$ cSt, suggesting that they should be able to cloak the water drops and the interface between the droplet and the SHS as well due to their low viscosity in about 0.5ms. In contrast, the high viscosity oil would take about 50ms to cover the entire droplet and around tens of milliseconds to cloak the interfacial area between the droplet and the SHS. Given that the entire retraction phase occurs in about 10-20ms this might not be enough time for a highly viscous oil to be able to suppress rebound.

*2.1.6 Practical embodiment*

We have demonstrated that oil cloaking is an extremely simple, effective and robust method to promote droplet retention on superhydrophobic surfaces. Having explored a wide regime of fluidic and interfacial parameters with single droplet impacts, we sought to implement our knowledge into a practical device that could be used to demonstrate practical enhancements to spray retention. We developed a prototype that involved two nozzles, one for the water and another for the oil. (see Methods)

To test the ability of our sprayer to enhance retention in the most extreme case, we sprayed both water and soybean oil – cloaked water droplets onto a large OTS- nanograss surface. In order to measure retention performance in terms of mass, we weighed the retained mass of droplets in both cases. Figure 15a shows a photograph of the end result of spraying water drops onto the surface for 3 seconds. As expected, almost all the water drops sprayed onto the superhydrophobic surface bounce off (see Supplementary movie 15). Figure 15b shows a photograph of the end result of spraying water drops cloaked in ~ 1 wt % soybean oil for 3 seconds. Almost immediately after spraying commences, the water drops begin sticking to the surface (see Supplementary movie 16) and by the end of 3 seconds, we measure a 96x enhancement in retained mass (Figure 15c) for the case of soybean oil. Figure 15c also shows retention data for experiments where oil cloaked droplets were only sprayed for 1 and 2 seconds. We find that this trend is consistent for other vegetable oils that are commonly used in agriculture such as canola or cotton seed oil, illustrating the robustness of our approach [98,99]. These experiments show the potential of this technology to greatly reduce the amount of pesticides sprayed as with even a third of the spray time, the technique allows for 7.3x-14x enhancements in mass retention based on the oil used. Crucially, these enhancements are achieved with oils that are inexpensive, widely used and safe for the environment, farm workers and crops. These oils are also known to be widely compatible with pesticide chemistries, delay evaporation of agrochemical spray droplets and promote foliar uptake of pesticides [75,96].

In figure 11, we demonstrated the ability of our prototype sprayer to reduce spray waste in terms of surface coverage on leaves. In order to demonstrate the ability of our sprayer

to enhance the retained mass, we spray 3 more crop leaves (kale, spinach and lettuce) and the end result of 1s of spraying on all the leaves is shown in figure 15d-g. The total retained mass of droplets is normalized by the area of the leaf and the spraying time for both water and soybean oil cloaked droplets and is presented in figure 15h. We observe >3x enhancements in normalized retained mass across leaves demonstrating the wide practical applicability of our approach in enhancing droplet retention.

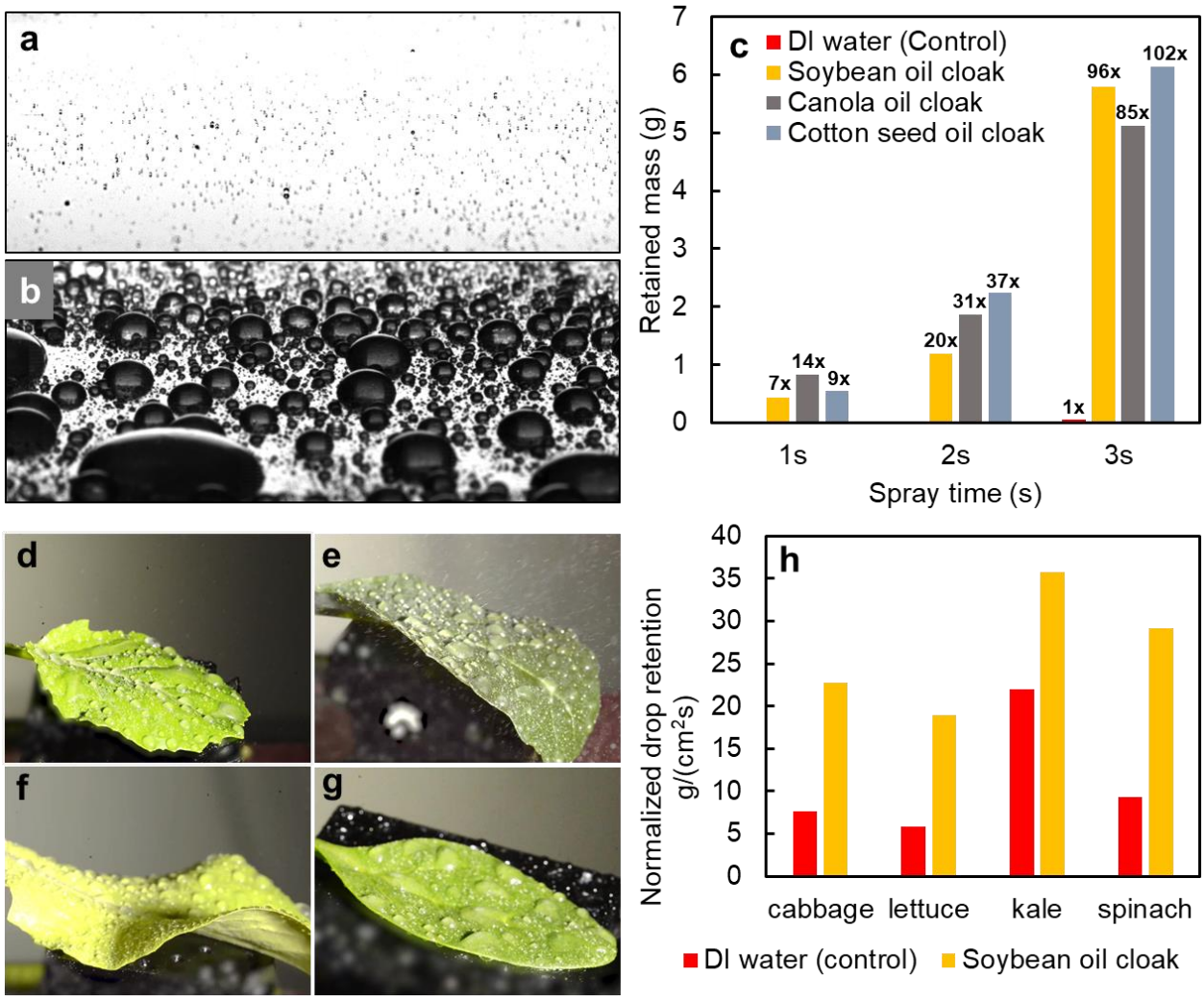


Figure 14: Water and oil-cloaked water droplets sprayed on a superhydrophobic surface and different crop leaves. (a) The end result of spraying a 6-inch superhydrophobic wafer with pure water through a conventional agricultural spray nozzle for 3 seconds (see Supplementary Movie 7) (b) The same wafer after 3s of spraying oil cloaked (1% by volume - soybean oil) droplets generated by the same spray nozzle (see Supplementary Movie 8). (c) Retained mass of droplets on the engineered superhydrophobic surface for different spray times and different oil cloaks. (d-g) Snapshots to demonstrate the coverage attainable with 1 second of spraying with soybean oil-cloaked droplets on (d) cabbage, (e) kale, (f) lettuce and (g) spinach leaves. (h) Mass of droplets retained on the leaf normalized by leaf area and spray time are compared on 4 crop leaves for pure water and soybean oil cloaked droplets (~ 1 wt%)

## 2.3 Conclusions and Outlook

In conclusion, we have demonstrated a simple, environmentally sustainable, inexpensive and effective approach to enhance the retention of sprays on hydrophobic and superhydrophobic surfaces. By cloaking droplets in minute quantities of oil (<1% by volume), we were able to demonstrate robust rebound suppression on two types of superhydrophobic surfaces with 9 different oils that span a wide range of viscosities and surface tensions across agriculturally relevant impact conditions. We were able to demonstrate the rebound suppression with as little as 0.1% oil by volume per droplet. By modeling the viscous and surface energy-based dissipation during the impacts of these cloaked droplets, we were able to provide a physical understanding of the rebound suppression across our experiments. Finally, we translated these findings into a prototype sprayer which was able to demonstrate up to a 102x enhancement in retention on superhydrophobic surfaces and up to a 5.25x reduction in waste when spraying on crop leaves. These enhancements were achieved using food and environmentally safe vegetable oils and the methodology presented here demonstrates great promise in reducing the human health and environmental impact of pesticides.

## 2.4 Materials and Methods

### *2.4.1 Impact velocity, center of mass, and coefficient of restitution estimation*

Impact velocity and Center of Mass (COM) data was extracted from the high-speed videos via image analysis of each frame. Care was taken when lighting the background and surface such that the edges of the droplet were the darkest features of the video. This enabled the use of a simple thresholding method to create a mask of droplet's outline. For each row of pixels in the droplet mask, the width of the mask was taken to be the local diameter of the droplet under the assumption that the droplet remained axisymmetric at all times. The partial mass of each row was calculated as the mass of a disk one pixel thick. The mass-average of these partial masses weighted by their vertical position yielded the COM. The impact velocity was calculated by differentiating the frame-by-frame vertical COM with respect to time and taking the velocity just before impact. Because the rebound velocity of a droplet is highly variable throughout the rebound process, an alternative definition of the coefficient of restitution was established, where $e_o = \frac{\sqrt{2gh_{COM}}}{v_i}$. By using the maximum COM height of the droplet after rebound to calculate an equivalent velocity, a much more reliable value is obtained.

### *2.4.2 Practical embodiment setup*

In order to test the coverage of leaf surfaces by an agriculturally relevant spray, a reservoir of deionized water was pressurized at 2 atm (30 psi) and flowed through a TG-1 TeeJet

Full Cone Spray Tip (Spray Smarter), with the resulting spray directed at the leaf. A distance of approximately 75cm was maintained between the sprayer and leaf. An AA250AUH Automatic Spray Nozzle (Spraying Systems) was installed just upstream of the spray tip to control the spray time by switching on and off. The water droplets from the primary nozzle were cloaked in oils using a secondary airbrush sprayer. Care was taken to ensure that the overlap angle of the two nozzles ensured that none of the oil from the secondary sprayer contaminated the surfaces directly. The flow rates of both fluids were controlled to ensure 1wt% cloaking.

### *2.4.3 Hydrophobizing needles*

The stainless-steel needles were hydrophobized by submerging them for 24 hours in a solution of 5mM Fluoroalkyl(C10) phosphonic acid (SP-06-003, obtained from Specific Polymers) solvated in methanol. A flat stainless-steel control surface subjected to the same conditions had a water-air contact angle of $>90^{o}$ confirming successful hydrophobization.

### *2.4.4 Contact angle measurements*

Contact angles were measured using a Ramé-Hart contact angle goniometer.

### *2.4.5 Confirming low volume fractions of oil*

All the volume fractions of oil were confirmed by measuring the weights of dispensed liquids over time.

## 2.5 Supplementary figures

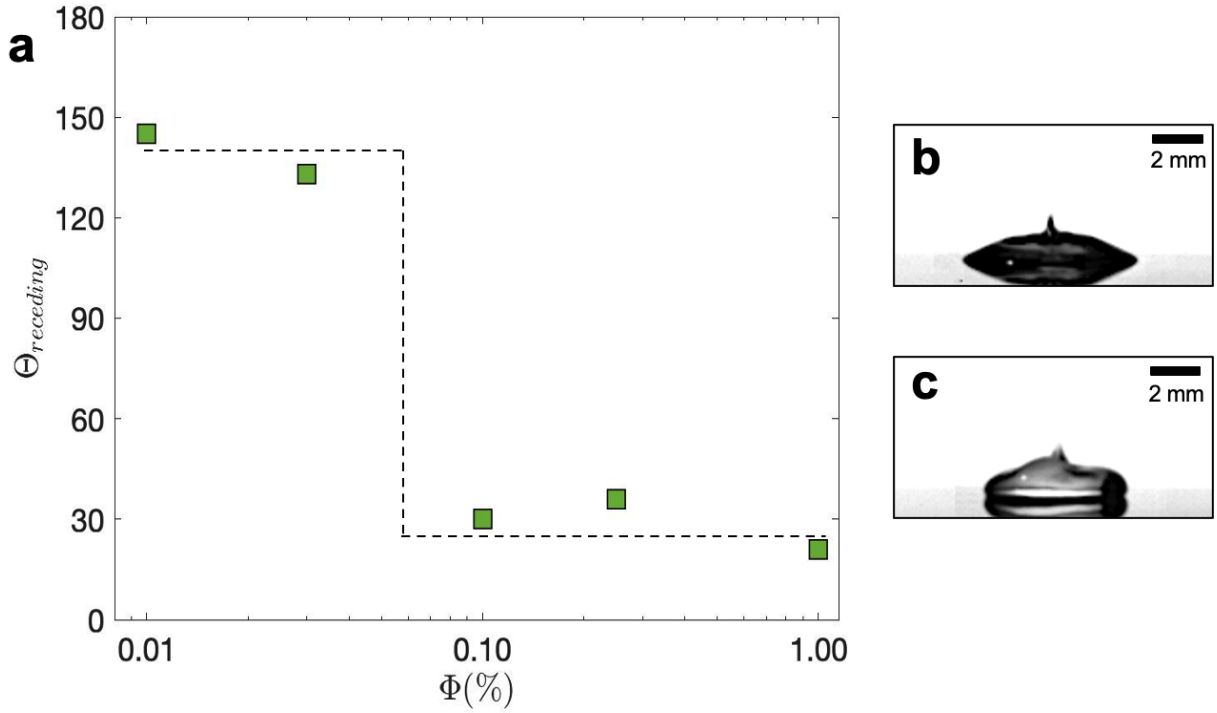


Figure S1: (a) Average dynamic contact angle measured during the retraction phase for water droplets cloaked in 10cSt Silicone oil at the low oil volume fractions shown in Figure 4. The increase in retraction contact angle at 0.03% oil fraction accompanies the increase in restitution coefficient observed in Figure 12, indicating that at sufficiently low oil fractions the oil can no longer pin the contact line and suppress droplet rebound. (b) and (c) are snapshots taken during the retraction of oil cloaked droplets with 0.10% and 0.03% oil by volume, respectively, demonstrating the markedly different contact angle.

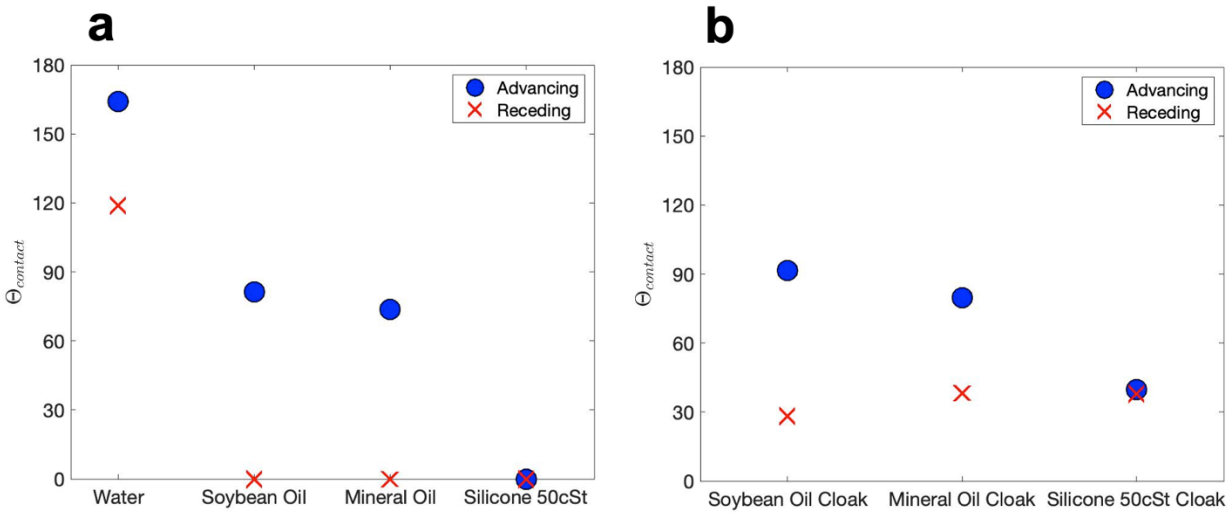


Figure S2: Advancing and receding contact angles of water and cloaking oils on the engineered superhydrophobic surface. Measurements were obtained by gently placing a droplet on the surface and dispensing fluid into or withdrawing fluid from the droplet to measure advancing and receding angles, respectively. These measurements were performed for (a) homogenous liquid drops composed of only oil or only water and (b) oil-cloaked water droplets (1% oil by volume).

# Chapter 3: Enhanced $CO_2$ absorption via mists and space charge injection

## 3.1 Introduction and Background

Global $CO_2$ emissions reached 36Gt in 2019, placing an enormous strain on the Earth's climate [119,120]. Post combustion carbon capture in power plants offers an efficient pathway to reducing anthropomorphic emissions as capturing the $CO_2$ produced by a single 500MW natural gas power plant over a year would be equivalent to eliminating emissions from two hundred thousand cars over the same timespan [121,122]. Post-combustion carbon capture technologies can be classified into three main approaches: chemical, physical and biochemical [123–125]. Chemical approaches include adsorption, direct or membrane-assisted absorption into a liquid, and chemical looping combustion [126–130]. Physical approaches include membrane separation, physical absorption and cryogenic distillation [131–133]. More recently a variety of biochemical methods utilizing enzymatic and algae-based approaches have also been proposed [134,135]. Of these methods, chemical absorption into a liquid absorbent is widely considered to be the most promising technology due to the higher efficiencies, lower costs and techno-economic maturity that it offers [123,124].

Most practical chemical absorption plants utilize packed bed reactors – an illustration of which is shown in figure 16a. These reactors are tall towers filled with a number of packing units. Sorbent solution is provided at the top of the tower and flows down over the surface of the packing units; forming films of liquid that react with the rising flue gas stream. The packing units are designed to enhance the interfacial area and the contact time between the flue gas and the liquid absorbent [136]. In order to capture >90% of the $CO_2$ released from a power plant (where flue gas flow rates can vary between 100-800 kg/s), packed bed reactors need to be large enough to provide enough area and time for absorption to take place [137–139]. As a result, packed bed towers are routinely over 10m in diameter and over 20m in height; contributing to approximately 30% of the overall capital requirements for such carbon capture systems [140,141]. With prohibitively expensive costs being the primary reason for only 28 large scale carbon capture facilities existing worldwide, reducing the size of these absorption towers would help enhance the practicality of post combustion carbon capture systems [142].

Spray towers theoretically provide a pathway towards much smaller absorber units. In spray towers, droplets of the absorbent are sprayed against the rising gas stream [143–145]. These droplets absorb $CO_2$ from the flue gas and are collected at the bottom of the tower. Equation set 1 demonstrates the enhancement to interfacial area afforded by droplets in comparison to the liquid films in packed beds.

$$\frac{A_p}{V} = \frac{1}{t};\ \frac{A_d}{V} = \frac{N4\pi R^2}{N\frac{4}{3}\pi R^3} = \frac{3}{R};\ \frac{A_d}{A_p} = \frac{3t}{R} = \frac{6t}{D} \quad (1)$$

In the above equations, $A_p$ is the area of the packed bed, $V$ is the volume of the liquid absorbent, $t$ is the thickness of the liquid film in the packed bed, $A_d$ is the area of the droplets that would make up the same volume of absorbent, and $R$ and $D$ are the droplet radius and diameter respectively. For the same characteristic length, droplets offer 6 times more interfacial area than films in packed beds [137,139,146]. Despite this advantage, in practice, spray towers offer lower $CO_2$ capture efficiencies than packed beds. There can be droplet loss to the walls of the reactor which reduces the overall $CO_2$ capture efficiency [143]. Conventional spray towers are counterflow systems and thus rely on gravity to collect the absorbent droplets. The drops cannot be smaller than a few hundred microns as they could be entrained by the flue gas and escape through the exhaust. While passive demisters could be considered, they tend to fail at high liquid loading rates and introduce unfavorable back pressures to the exhaust system [147,148]. This means that the benefit of high interfacial area cannot fully be exploited in conventional spray towers. Droplets that are too large also present a problem as such droplets have slower reaction rates and fall faster through the tower.

Here we propose a two-stage system (shown in figure 16b) to leverage the advantages offered by droplets to a greater extent. In the first – absorption stage, we propose using mist-scale droplets with diameters between 15 and 50 µm, which would allow our system to achieve up to a 280-fold increase to the interfacial area available between the absorbent and the gas compared to packed bed reactors. While this could allow for absorber units that are significantly shorter, droplets of this size will be easily entrained by the gas flow. In order to capture this large liquid volume, we propose a second – electrostatic droplet capture stage. Specifically, by utilizing a corona discharge, we will charge the mist-scale droplets and introduce an electrical force that will drive them to a collector from where the liquid absorbent can be collected, processed and recirculated [149,150].

To better understand the ability of our proposed system to reduce the overall size of absorbers, we theoretically estimate the lengths required for both stages of our system. We can model $CO_2$ absorption into droplets of different radii using an existing empirical model as shown in equation 2 which was developed by Choi et al. [151]. Since the benefits afforded by our proposed system are agnostic of the specific absorbent chemistry, we will utilize ammonia as a model absorbent.

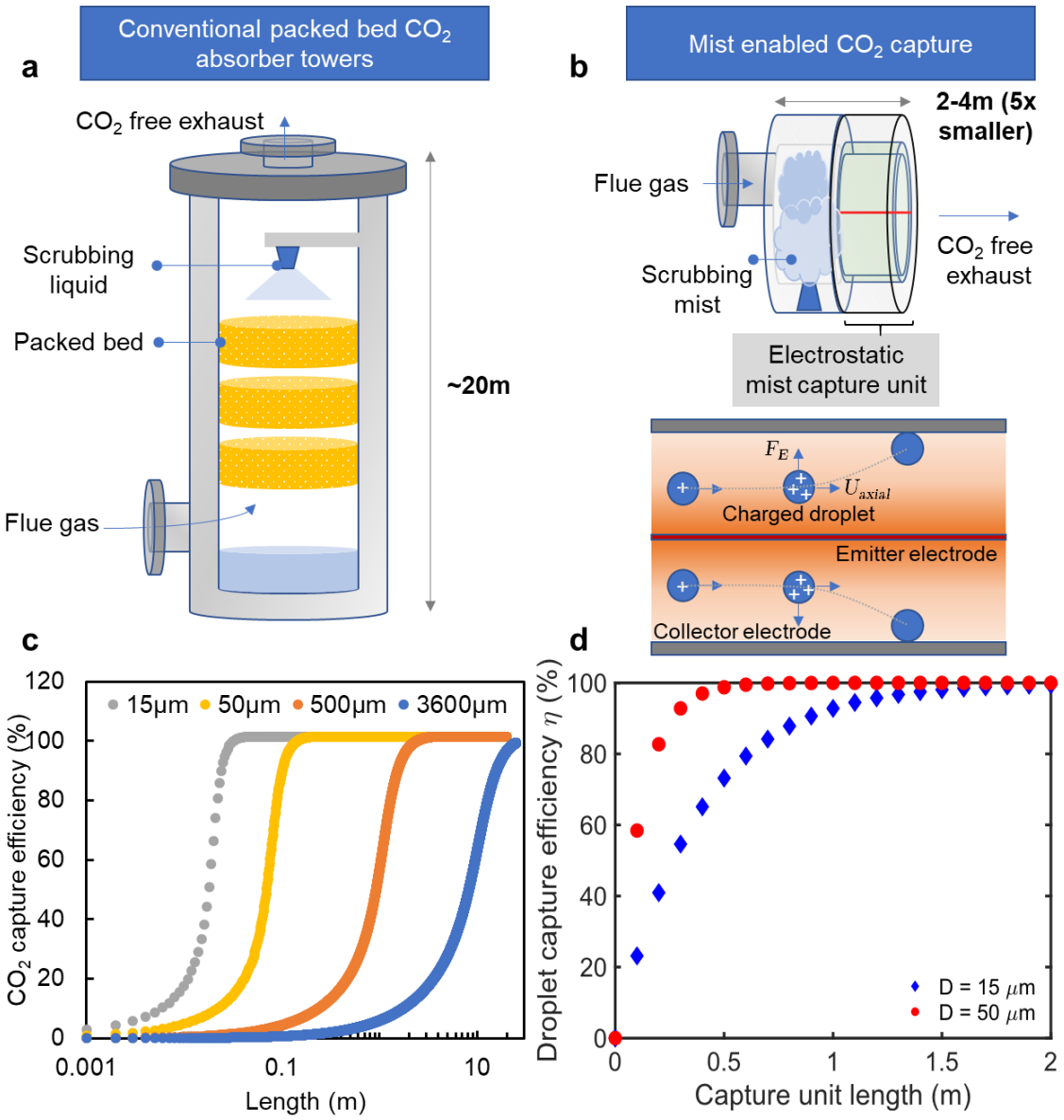


Figure 15: Mists can enable significantly cheaper $CO_2$ capture systems. (a) Conventional absorption towers use tall towers (10-20m in height) and packed beds to enhance the interfacial area and the residence time of the scrubbing liquid and the flue gas during absorption. (b) Misting the scrubbing fluid would allow for significantly shorter absorbers due to higher interfacial areas afforded by small droplets, however such mists are difficult to capture and recycle using passive demisters. An active electrostatic demister can capture these mists without imposing significant back pressures. (c) Calculated $CO_2$ capture efficiency for mist-based CO2 capture as a function of absorber length and droplet size for a liquid to gas mass flow ratio of 1:1 using a single droplet model from literature [151]. (d) Calculated mist capture efficiency for an electrostatic demister unit as a function of length for different average mist droplet diameters.

$$\frac{\dot{m}_{CO_2,j}}{A} = k^{0.48}\, C_{g,s,j} C_{l,j} \left[ \frac{2.15 \times 10^{-6}}{C_{l,i}^{0.5}} + \frac{1.4 \times 10^{-7}}{D^{0.3}} \left( 1 - \frac{C_{l,j}}{C_{l,i}} \right)^{2.5} \right] \quad (2)$$

In the above equation. $\dot{m}_{CO_2}$ is the mass flux of $CO_2$ into the droplet, $A$ is the droplet area, $k$ is the reaction rate, $C$ represents concentration, and $D$ is the droplet diameter. The subscripts, $g$ and $l$ represent the $CO_2$ and the sorbent respectively. The subscripts $s$ and $i$ represent the surface of the droplet and the inlet respectively and $j$ is an iteration counter. Using a gas flow velocity of 3 m/s, an inlet $CO_2$ concentration of 15% and an ammonia concentration of 15wt%, we can estimate the $CO_2$ absorbed by a single droplet from its sphere of influence as a function of droplet travel distance. We use a liquid-to-gas mass flow ratio of 1:1 to define the control volume that follows an individual droplet as it travels with the gas flow. Using this framework, we can examine the benefit theoretically afforded by our approach for droplets of different sizes [140]. Since absorbent films in packed bed reactors are typically 600-700 µm thick, we can replicate the interfacial area offered by packing units with a droplet diameter of 3600µm for a given volume of liquid [139,146]. We observe, that such large droplets would also require absorber towers that are >20 m tall, confirming the role of interfacial area in absorption. In contrast, when we move to droplet diameters of 50µm and 15µm, the required lengths for >95% CO absorption reduce significantly. In practice, the length of the absorption stage will be markedly larger than the dimensions predicted by the single drop model presented in figure 16c as the model doesn't account for droplet-droplet interactions, local concentration gradients and for the practical constraints of introducing up to 800 kg/s of absorbent into a flue gas stream. However, the model does show that drastic reductions to absorber dimensions are possible by transitioning to mist-scale droplets.

For the second stage of our system, we can also estimate the maximum length required to capture >95% of the mist droplets. Considering the cylindrical design of our electrostatic collector shown in figure 16b we can compare the electrostatic force that a charged droplet would experience with the aerodynamic drag force. We estimate the characteristic radial velocity ($U_r$) of a mist-scale droplet as shown in equation 3. Using the Deutsch-Anderson equation (equation 4), we can then estimate the droplet collection efficiency ($\eta$) as a function of cylinder length ($L_c$), diameter ($D_c$) and gas flow rate ($Q$) as shown in figure 16d [149,152–154].

$$U_r \sim \frac{qE}{6\pi\mu R} = \frac{4\pi R^2 \varepsilon_0 E^2}{6\pi\mu R} = \frac{2R\varepsilon_0 E^2}{3\mu} \quad (3)$$

$$\eta = 1 - e^{\left(-\frac{U_r A_c}{Q}\right)} = 1 - e^{\left(-\frac{U_r \pi D_c L_c}{C_{DA} Q}\right)} \quad (4)$$

In the above equations $q$ represents the charge accumulated on a single droplet, $E$ represents the electric field strength, $\mu$ is the viscosity of the flue gas, $R$ is the droplet radius, $\varepsilon_0$ is the permittivity of free space and $C_{DA}$ is the correction factor to the Deutsch-Anderson equation used for practical systems [149].

From figure 16c and 16d we see that the overall length of the absorber unit could be reduced from around approximately 20m in packed bed reactors for a 400MW power plant to less than 4m in the system proposed here [140]. This would enable a drastic reduction to the capital required for $CO_2$ absorber units [141]. To validate these models, we develop and test a scaled down version of our two-stage design. For the first stage of our system, we match the gas flux of industrial absorber units and study the effect of input $CO_2$ and catalyst concentration on $CO_2$ capture efficiency. For the second stage, we explore the droplet capture efficiency of a scaled down electrostatic system as a function of gas flow rate and the electric field strength. Finally, we present an economic analysis to capture the reduction to plant capital expenditure that could be enabled by our mist-based system.

## 3.2 Results and Discussion

### *3.2.1 Experimental setup*

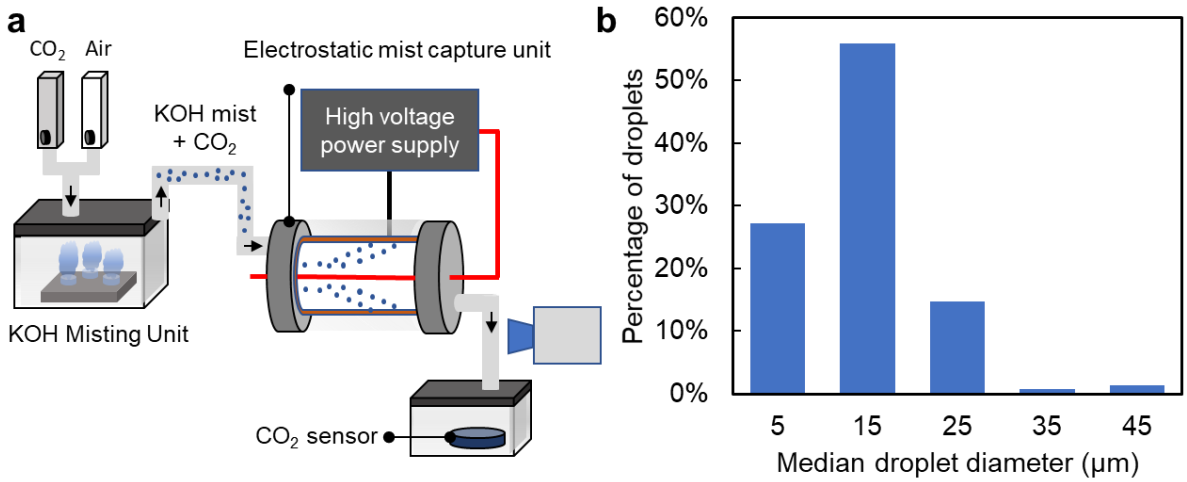


Figure 16: Scaled down experimental setup for mist-based $CO_2$ capture (a) $CO_2$ was mixed with air at various ratios and introduced into a misting unit. The catalyst (KOH) mist was entrained by the gas flow and proceeded to absorb the CO2 in the gas stream. The mist laden gas flow was then directed to an electrostatic capture unit before exiting into a CO2 sensor that measured $CO_2$ capture efficiency. (b) Histogram of droplet

parameters generated by the misting unit indicate that a majority of droplets fall within a diameter range of 10-20 µm.

Figure 17a presents an illustration of the experimental setup used in this work. Flow controlled $CO_2$ and air streams were mixed to achieve desired concentrations of $CO_2$ at the inlet to the system. The gas was then introduced to a misting unit where droplets were entrained into the gas flow (see Materials and Methods section). In our setup, potassium hydroxide was used as the absorbent due to experimental simplicity. The gas and the entrained mist then flowed through a fixed length of piping to allow time for absorption. The mixture then flowed into the electrostatic demister unit where all the absorbent drops were removed. Finally, an infrared $CO_2$ sensor was used to quantify the $CO_2$ captured in the system. Figure 17b shows a histogram of droplet diameters produced by our misting unit. This histogram was obtained by visually recording the mist droplets as the passed through the viewing window when the electrostatic droplet capture unit was turned off. This gave us an accurate representation of the droplets that were being entrained by the gas flow.

*3.2.2 Absorption stage*

In order to appropriately scale down our experimental absorber, the flow rate of the inlet gas was varied between 1 and 5 lpm while keeping the $CO_2$ concentration constant at 50%. Figure 18a shows the $CO_2$ capture efficiency of the system for these experiments. We observe that while the capture efficiency reached ~$74 \pm 5\%$ for the flowrates of 1 and 3 lpm, it dropped down to about $64 \pm 5\%$ for the 5 lpm case. To characterize this reduction in performance, we normalize the gas flux through our experimental setup by the flux

achieved in industrial absorption systems [155]. We do this, as industrial absorber systems are carefully designed to optimize the gas flux to achieve the maximum capture efficiency possible. In figure 18b, we plot the ratio of the experimental and the industrial gas fluxes and find that the case of 5 lpm has an unfavorable flux ratio which could explain the drop-in performance.

Setting the flow rate to 3 lpm, to stay in a favorable flux regime for the remaining absorption experiments, we varied the input $CO_2$ concentration from approximately 17% to 50% as shown in figure 18c. In all of these cases, we observe a capture efficiency of approximately $70 \pm 5\%$ which is consistent with other industrial KOH-based absorption units [156]. The liquid to gas mass flow ratio (L/G) of was measured to be approximately $21 \pm 4$ for a gas flow rate of 3 lpm and this value is also of the same order as industrial and other experimental systems [143,156].

Equation 5 shows the stoichiometric reaction between KOH and $CO_2$. In our experimental setup, at a gas flow rate of 3 lpm, the molar flow rates of KOH and $CO_2$ are 1.7 and 1.1 milli-moles per second. Since two moles of KOH are needed to react with every mole of $CO_2$, the stoichiometric capture efficiency is 76%. To validate that the $74 \pm 5\%$

experimental capture efficiency observed here is indeed limited by the chemical concentration of the absorbent, we increase the KOH concentration from 1M to 2M and observe that the $CO_2$ capture efficiency increases to 95 ± 5% for the case of a 3 lpm gas flow rate and a 50% inlet $CO_2$ concentration. These results illustrate the promise of mist-based carbon capture, especially in terms of enabling a wider range of absorbents that

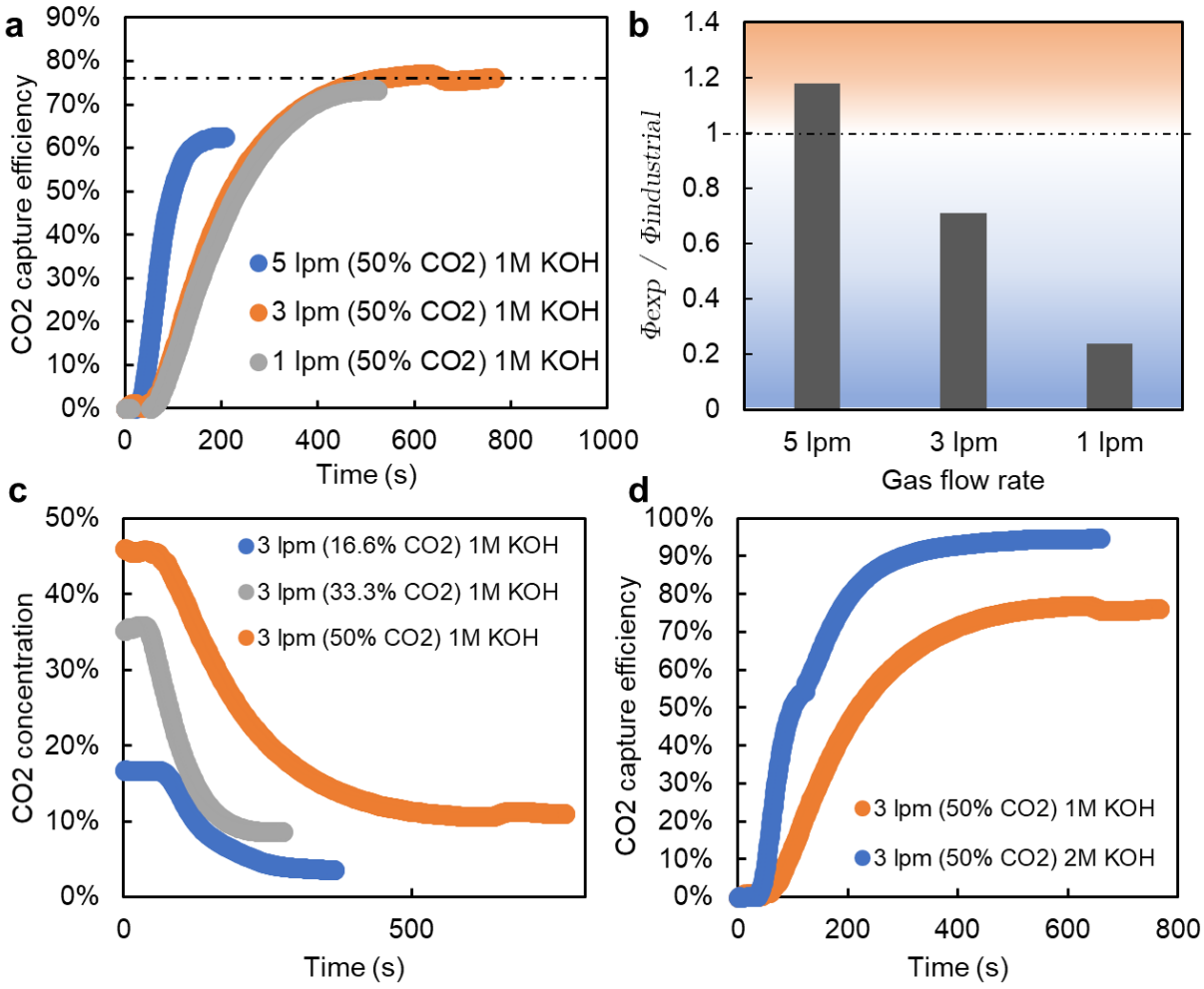


Figure 17: Mists enable high absorption efficiencies. (a) CO2 capture efficiency is plotted as a function of time after the misting unit is switched on for varying gas flow rates, and an input CO2 concentration of 50%. At a gas flow rate of 5 lpm, the capture efficiency drops from 75 ± 5% to 64 ± 5 % indicating that that the liquid to gas ratio and the residence time are too low for the scrubbing to be maximally effective. (b) A comparison of normalized gas flux in kg/m$^2$s of our experimental setup and industrial systems further confirms that in the 5 lpm case, the flow rate of the gas is too high to optimize $CO_2$ capture. (c) Demonstrates the effect of varying the CO2 concentration while holding flowrates constant. In these experiments, all the capture efficiencies were $>$ 70% demonstrating the ability of the technique to be robust to input $CO_2$ concentrations and

demonstrating that at these conditions, the capture efficiency is limited by absorbent chemistry (d) Illustrates the effect of changing absorbent chemistry by plotting the CO2 capture efficiency for different concentrations of the catalyst (KOH). Up to 95% capture efficiency can achieved with 2M KOH solution. The liquid to gas flow ratio was measured to be 21 ± 4 for these experiments in the case of 3 lpm gas flow rate.

could have a better environmental and safety profile than the alcoholic amines that are currently preferred in absorber units [124].

$$2KOH + CO_2 \rightarrow K_2CO_3 + H_2O \tag{5}$$

*3.2.3 Mist droplet capture stage*

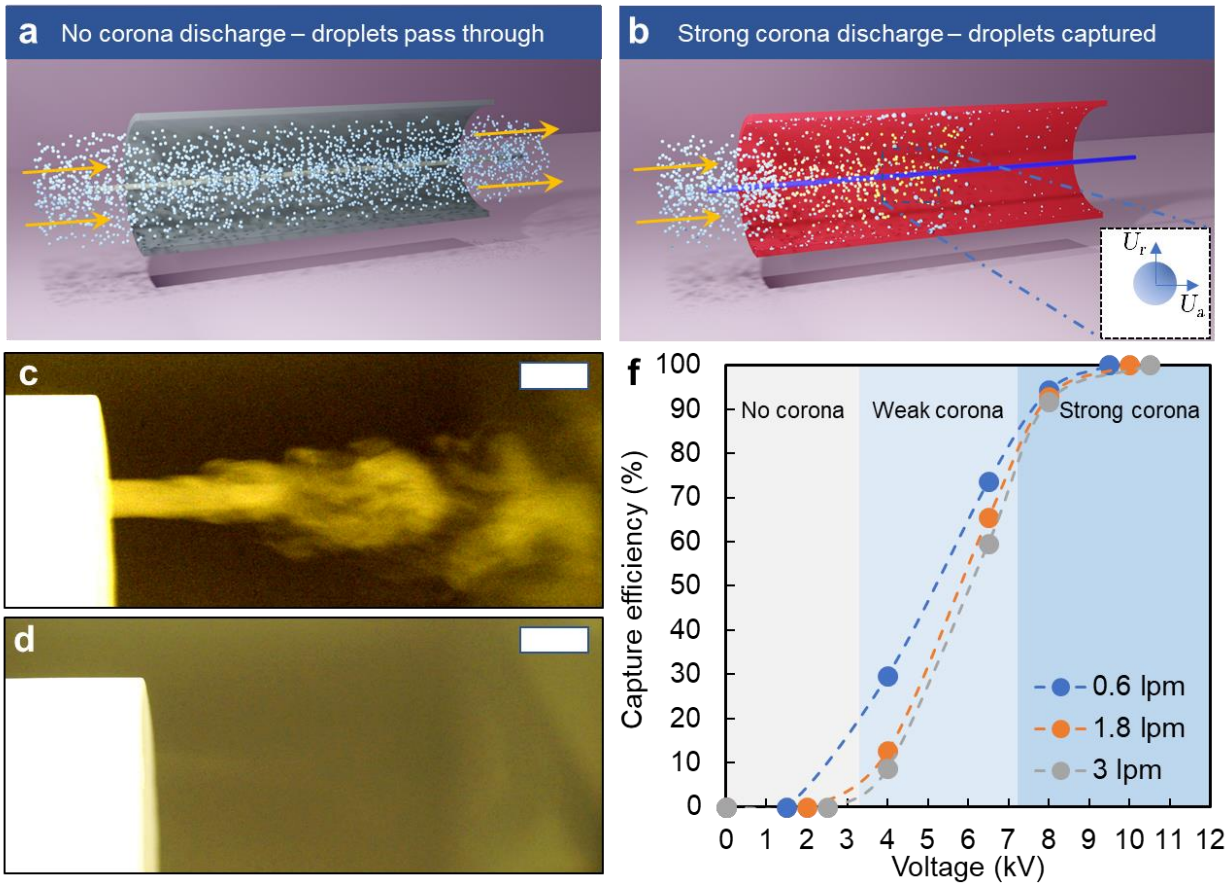


Figure 18: Capturing mist using space charge injection (a,b) Conceptual schematics of the mist capture system in the off and on states. (c,d) Photographs corresponding to the extreme states tested in the mist capture unit. The scale bar is 1 cm wide. When the voltage source is off, mist exists the misting unit as it is entrained by the gas flow, but when the emitter electrode produces a strong corona discharge, all the mist is captured. (d) The droplet capture efficiency is plotted as a function of the applied voltage and for

different gas flow rates, illustrating the ability of our active approach to efficiently capture mist.

Having demonstrated the ability of mist-scaled droplets to achieve $CO_2$ capture efficiencies >70 % we explore the ability of our scaled down electrostatic unit to capture the mist droplets. Figure 19a and 19b show conceptual schematics of the mist capture unit when there is no corona discharge and when there is a stronger discharge respectively. Figure 19c and 19d show digital photographs of the exit of the demisting unit under no corona and strong corona conditions, visually illustrating the ability of our scaled-down demister to completely capture mist for a gas flow rate of 3lpm and a voltage of approximately 8 kV. Figure 19f shows the mist capture efficiency as a function of gas flow rate and applied voltage. When the voltage isn't high enough to the generate a corona discharge, the droplets aren't charged and therefore don't get collected. As the voltage is increased, we pass the corona onset voltage and begin to collect droplets. In this state, the concentration of free ions in the gas stream isn't high enough to charge all the mist-scale droplets that are entrained and therefore we only achieve partial capture. In the region of strong corona, we are able to achieve 100% capture as nearly all the droplets become charged and are transported to the grounded collector. The electric field strength applied in our scaled down system is about 2 KV/cm which is well within the field strength used in scaled-up electrostatic precipitation systems indicating the practical promise of our two-stage system [149].

*3.2.4 Economic Analysis of a scaled-up absorber unit*

Our experiments show that when our two-stage absorber is appropriately scaled down, we can achieve $CO_2$ capture efficiencies between 70-95% and that all the mist droplets can be captured effectively. To assess the economic feasibility of our mist-based post combustion carbon capture approach, we estimate the required capital expenditures (CAPEX) to install our system and compare it to the CAPEX required for a conventional vertical packed bed absorber tower. For the conventional vertical packed bed architecture, two absorber towers of heights 19.06m and diameters of 11.93m are chosen from an optimized MEA $CO_2$ capture system for a 400MW gas-fired power plant with a flue gas rates of 622 kg/s [140]. Purchased costs of the absorber tower housing and the internal components are estimated from average historical data and subsequently adjusted via the Chemical Engineering Plant Cost Index (CEPCI) to 2019 USD [157]. A typical Lang Factor of 4.74 was applied to yield the estimated installed cost of the system components tabulated in Table 1.

The estimated total CAPEX for the packed bed system is $149M, which agrees with values estimated by Agbonghae et al. for the same absorber configuration [140,141]. As expected, the stainless steel-clad carbon steel absorber tower is a key cost driver, accounting for over 50% of the cost. To estimate an analogous CAPEX for our mist-based $CO_2$ absorption system, the same flue gas flow rate and absorber unit housing diameter

were used as in the previous case. By leveraging the enhanced absorption kinetics of mists, the absorber housing unit length can be reduced by a factor of 5x as shown earlier. Moreover, it can be installed in a horizontal configuration as it no longer uses gravity-driven flows, thereby reducing installation cost factors. The costs of the electrostatic mist capture unit are derived from historical costs and installation factors, scaled for capacity, and adjusted with the CEPCI index [158]. At a CAPEX of $57.3M, our mist-based $CO_2$ absorption system offers a ~2.6x reduction in capital cost compared to conventional packed bed absorption towers. These savings are due to the elimination of the packed beds in addition to a reduction in absorber unit housing costs associated with smaller total dimensions.

| Subsystem description | Packed Bed Architecture Cost ($USD MM) | Mist Capture Architecture Cost ($USD MM) |
|---|---|---|
| **Absorber unit - CAPEX** | | |
| Absorber unit housing | 81.3 | 9.0 |
| Packed Bed | 57.9 | -- |
| Liquid nozzles | 4.9 | 3.8 |
| Pressure pumps | 2.8 | 3.4 |
| **Mist capture system - CAPEX** | | |
| Passive de-misting | 2.5 | -- |
| Space charge capture | -- | 42.6 |
| **Total CAPEX** | **149.4** | **57.3** |

Table 1: $CO_2$ absorption capital expenditure estimates for a 400MW gas fired coal plant for conventional vertical packed-bed architectures compared to the proposed mist-capture architecture. Owing to the substantial reduction in absorber unit housing size and the avoidance of packed beds, the mist capture architecture has a CAPEX ~2.6x lower than conventional packed bed architectures. Costs are based on historical pricing (Turton et. al) and scaled accordingly for their capacity, material selection, and operational pressures.

## 3.3 Conclusions and Outlook

In conclusion, we have demonstrated a simple, yet efficient proof-of-concept absorber system to capture $CO_2$ using mist-scale droplets. Using a scaled down experimental setup that matches the gas flux and L/G ratios of other industrial and experimental post combustion carbon capture systems, we were able to achieve $CO_2$ capture efficiencies up to 95% using potassium hydroxide as the absorbent. We were also able to demonstrate the ability of our electrostatic droplet capture unit to collect $> 95\%$ of the entrained droplets at an electric field strength that is consistent with industrial systems. Finally, we use chemical engineering plant economic models to estimate that a scaled-up installation of the proposed system could reduce $CO_2$ absorber costs by a factor of 2.6. While these

results are promising there are experimental avenues to explore before the methodology can be validated for scaled up use. Making the L/G ratio independent of the gas flow rate would allow for the exploration of lower liquid fractions and help benchmark the performance under a wider range of industrially relevant operating conditions. Secondly, testing the system with other absorbents would help develop models that can more accurately predict absorption efficiency as a function of length by taking droplet interactions into account. While such efforts and experiments that can more accurately capture the flow conditions inside flue gas streams would greatly improve understanding, the concept, framework and experimental results presented in this work prove the promise of using mist-scale droplets for CO2 capture.

## 3.4 Materials and Methods

### *3.4.1 Gas mixing and mist generation*

Brooks® mechanical flow meters were used to control the flow rates of the $CO_2$ and air before the two gas streams were mixed using a T-junction. The mixed gas was introduced into the headspace of an air-tight container that contained a bath of the absorbent and an ultrasonic misting unit (Mxmoonant® 6 Head Ultrasonic Mist/Fog maker). The experiments were started with the misting unit and the mist capture units turned off. The initial concentration of the $CO_2$ was recorded after the gas flowed through the headspace of the air-tight container so that any effects of the bath of absorbent were considered in the control measurement. When the ultrasonic mister was turned on, mist scale droplets were ejected into the headspace of the air-tight container and subsequently entrained by the gas flow.

### *3.4.2 $CO_2$ sensor*

$CO_2$ concentrations were measured using a GC-0007 ExplorIR® sensor. The sensor was placed in line with the gas stream in a vented container.

# Conclusion

In this work, we explored how engineering physico-chemical interactions by introducing new interfaces or interfacial forces can be leveraged to achieve efficiency enhancements in a wide range of phenomena.

In Chapter 1 we demonstrated a simple, yet efficient technique to enhance the injectability of highly concentrated and viscous biopharmaceuticals using core annular flows. We established a regime map of flow rates and viscosity ratios required to attain stable core annular flow while minimizing the flow rate of the lubricant. We found that significant pressure reduction can be achieved in core annular flows for a variety of payload viscosities. We initially achieved up to a 7x reduction in pressure for a viscosity ratio of 33. In addition, we examined the role of buoyancy-induced eccentricity and compared our measurements to predicted pressure reduction in such eccentric core annular flows. We found that this model accurately captures the results of our experiments. We applied this knowledge to design, fabricate and test a first-generation prototype syringe. We showed substantial pressure reduction (up to 5x reduction for $\lambda = 26$) in our syringe which is consistent with our eccentric flow model, therefore significantly expanding the regime of injectable viscosities for biologics without increasing costs, risk of cross-contamination or manufacturing complexity by itself. We then examined the role of convection and eccentricity timescales in mitigating buoyancy effects and demonstrated viscosity agnostic injectability. We demonstrate manually applicable injection forces for formulations with viscosities up to 500cP. Finally, we implement these learnings into the design of an easy-to-manufacture second generation prototype.

Chapter 2 explored a simple, environmentally sustainable, inexpensive and effective approach to enhance the retention of sprays on hydrophobic and superhydrophobic surfaces. By cloaking droplets in minute quantities of oil (<1% by volume), we were able to demonstrate robust rebound suppression on two types of superhydrophobic surfaces with 9 different oils that span a wide range of viscosities and surface tensions across agriculturally relevant impact conditions. We were able to demonstrate the rebound suppression with as little as 0.1% oil by volume per droplet. By modeling the viscous and surface energy-based dissipation during the impacts of these cloaked droplets, we were able to provide a physical understanding of the rebound suppression across our experiments. Finally, we translated these findings into a prototype sprayer which was able to demonstrate up to a 102x enhancement in retention on superhydrophobic surfaces and up to a 5.25x reduction in waste when spraying on crop leaves. These enhancements were achieved using food and environmentally safe vegetable oils and the methodology presented here demonstrates great promise in reducing the human health and environmental impact of pesticides.

Finally, Chapter 3 presented a simple, yet efficient proof-of-concept absorber system to capture $CO_2$ using mist-scale droplets. Using a scaled down experimental setup that matched the gas flux and L/G ratios of other industrial and experimental post combustion carbon capture systems, we were able to achieve $CO_2$ capture efficiencies up to 95%. We were also able to demonstrate the ability of our electrostatic droplet capture unit to collect $> 95\%$ of the entrained droplets at an electric field strength that is consistent with industrial systems. Finally, we used chemical engineering plant economic models to estimate that a scaled-up installation of the proposed system could reduce $CO_2$ absorber costs by a factor of 2.6.

# Bibliography


1. *Pharmaceutical Research and Manufacturers of America. Medicines in Development — Biologics (2013 report). PhRMA [online], http://www.phrma.org/sites/default/files/pdf/biologics2013.pdf (2013).*
2. *Biotech products in Big Pharma clinical pipelines have grown dramatically.* (Tufts center for the study of drug development, 2013). doi:2013
3. Brekke, O. H. & Sandlie, I. Therapeutic antibodies for human diseases at the dawn of the twenty-first century. *Nat. Rev. Drug Discov.* 2, 52–62 (2003).
4. Awwad, S., Angkawinitwong, U., Awwad, S. & Angkawinitwong, U. Overview of Antibody Drug Delivery. *Pharmaceutics* 10, 83 (2018).
5. Kimiz-Gebologlu, I., Gulce-Iz, S. & Biray-Avci, C. Monoclonal antibodies in cancer immunotherapy. *Mol. Biol. Rep.* 45, 2935–2940 (2018).
6. Hviid, L. & Barfod, L. Malaria vaccines: immunity, models and monoclonal antibodies. *Trends Parasitol.* 24, 392–395 (2008).
7. Michaeli, D. Vaccines and Monoclonal Antibodies. *Semin. Oncol.* 32, 82–86 (2005).
8. Garidel, P., Kuhn, A. B., Schäfer, L. V., Karow-Zwick, A. R. & Blech, M. High-concentration protein formulations: How high is high? *Eur. J. Pharm. Biopharm.* 119, 353–360 (2017).
9. Narasimhan, C., Mach, H. & Shameem, M. High-dose monoclonal antibodies via the subcutaneous route: challenges and technical solutions, an industry perspective. *Ther. Deliv.* 3, 889–900 (2012).
10. Yadav, S., Shire, S. J. & Kalonia, D. S. Factors Affecting the Viscosity in High Concentration Solutions of Different Monoclonal Antibodies. *J. Pharm. Sci.* 99, 4812–4829 (2010).
11. Hung, J. J., Borwankar, A. U., Dear, B. J., Truskett, T. M. & Johnston, K. P. High concentration tangential flow ultrafiltration of stable monoclonal antibody solutions with low viscosities. *J. Memb. Sci.* 508, 113–126 (2016).
12. Sharma, V. K. *et al.* In silico selection of therapeutic antibodies for development: Viscosity, clearance, and chemical stability. *Proc. Natl. Acad. Sci.* 111, 18601–18606 (2014).
13. Tomar, D. S. *et al. In-silico* prediction of concentration-dependent viscosity curves for monoclonal antibody solutions. *MAbs* 9, 476–489 (2017).
14. Swanson, A. B., Matev, I. B. & de Groot, G. THE STRENGTH OF THE HAND. *Bull Prosthet Res* 10, 145–153 (1970).
15. Vo, A., Doumit, M. & Rockwell, G. The Biomechanics and Optimization of the Needle-Syringe System for Injecting Triamcinolone Acetonide into Keloids. *J. Med. Eng.* 2016, (2016).
16. Burckbuchler, V. *et al.* Rheological and syringeability properties of highly

concentrated human polyclonal immunoglobulin solutions. *Eur. J. Pharm. Biopharm.* 76, 351–356 (2010).

17. Arendt-Nielsen, L., Egekvist, H. & Bjerring, P. Pain following controlled cutaneous insertion of needles with different diameters. *Somatosens. Mot. Res.* 23, 37–43 (2006).
18. Mitragotri, S., Burke, P. A. & Langer, R. Overcoming the challenges in administering biopharmaceuticals: formulation and delivery strategies. *Nat. Rev. Drug Discov.* 13, 655–672 (2014).
19. Hoffman, P. ., Abuknesha, R. ., Andrews, N. ., Samuel, D. & Lloyd, J. . A model to assess the infection potential of jet injectors used in mass immunisation. *Vaccine* 19, 4020–4027 (2001).
20. Suriaa, H., Van Enk, R., Gordon, R. & Mattano, L. A. Risk of cross-patient infection with clinical use of a needleless injector device. *Am. J. Infect. Control* 27, 444–447 (1999).
21. Kelly, K. *et al.* Preventing contamination between injections with multiple-use nozzle needle-free injectors: A safety trial. *Vaccine* 26, 1344–1352 (2008).
22. Coffman, C. *et al.* Particles comprising a therapeutic or diagnostic agent and suspensions and methods of use thereof. (2017).
23. Qutachi, O. *et al.* Improved delivery of PLGA microparticles and microparticle-cell scaffolds in clinical needle gauges using modified viscosity formulations. (2018). doi:10.1016/j.ijpharm.2018.05.025
24. Whitaker, M. A., Langston, P., Naylor, A., Azzopardi, B. J. & Howdle, S. M. Particle size and shape effects in medical syringe needles: experiments and simulations for polymer microparticle injection. doi:10.1007/s10856-011-4359-7
25. Stickel, J. J. & Powell, R. L. FLUID MECHANICS AND RHEOLOGY OF DENSE SUSPENSIONS. *Annu. Rev. Fluid Mech.* 37, 129–149 (2005).
26. Oliemans, R. V. A. & Ooms, G. Core-Annular Flow of Oil and Water through a Pipeline. in *Multiphase Science and Technology* 427–476 (Springer Berlin Heidelberg, 1986). doi:10.1007/978-3-662-01657-2_6
27. Joseph, D. D., Bai, R., Chen, K. P. & Renardy, Y. Y. CORE-ANNULAR FLOWS. *Annu. Rev. Fluid Mech.* 29, 65–90 (1997).
28. Ghosh, S., Mandal, T. K., Das, G. & Das, P. K. Review of oil water core annular flow. *Renew. Sustain. Energy Rev.* 13, 1957–1965 (2009).
29. Strazza, D., Grassi, B., Demori, M., Ferrari, V. & Poesio, P. Core-annular flow in horizontal and slightly inclined pipes: Existence, pressure drops, and hold-up. *Chem. Eng. Sci.* 66, 2853–2863 (2011).
30. Nunes, J. K., Tsai, S. S. H., Wan, J. & Stone, H. A. Dripping and jetting in microfluidic multiphase flows applied to particle and fibre synthesis. *J. Phys. D. Appl. Phys.* 46, 114002 (2013).
31. Zhu, P. & Wang, L. Passive and active droplet generation with microfluidics: a

review. *Lab Chip* 17, 34–75 (2017).
32. Cubaud, T. & Mason, T. G. Capillary threads and viscous droplets in square microchannels. *Phys. Fluids* 20, 053302 (2008).
33. Zhang, Z. & Liu, Y. Recent progresses of understanding the viscosity of concentrated protein solutions. *Current Opinion in Chemical Engineering* 16, 48–55 (2017).
34. Shire, S. J. Challenges in the subcutaneous (SC) administration of monoclonal antibodies (mAbs). in *Monoclonal Antibodies* 131–138 (Elsevier, 2015). doi:10.1016/b978-0-08-100296-4.00006-3
35. Boger, D. V. Viscoelastic Flows Through Contractions. *Annu. Rev. Fluid Mech.* 19, 157–182 (1987).
36. Berteau, C. *et al.* Evaluation of the impact of viscosity, injection volume, and injection flow rate on subcutaneous injection tolerance. *Med. Devices (Auckl).* 8, 473–84 (2015).
37. Bentwich, M. Two-Phase Viscous Axial Flow in a Pipe. *J. Basic Eng.* 86, 669 (1964).
38. Bentwich, M., Kelly, D. A. I. & Epstein, N. Two-Phase Eccentric Interface Laminar Pipeline Flow. *J. Basic Eng.* 92, 32 (1970).
39. Yoshino, K. *et al.* Functional evaluation and characterization of a newly developed silicone oil-free prefillable syringe system. *J. Pharm. Sci.* 103, 1520–1528 (2014).
40. Foroughi, H. & Kawaji, M. Viscous oil–water flows in a microchannel initially saturated with oil: Flow patterns and pressure drop characteristics. *Int. J. Multiph. Flow* 37, 1147–1155 (2011).
41. Salim, A., Fourar, M., Pironon, J. & Sausse, J. Oil-water two-phase flow in microchannels: Flow patterns and pressure drop measurements. *Can. J. Chem. Eng.* 86, 978–988 (2008).
42. Ascarateil, S., Puget, A. & Koziol, M.-E. Safety data of Montanide ISA 51 VG and Montanide ISA 720 VG, two adjuvants dedicated to human therapeutic vaccines. *J. Immunother. Cancer* 3, P428 (2015).
43. Van Doorn, E., Liu, H., Huckriede, A. & Hak, E. Safety and tolerability evaluation of the use of Montanide ISATM51 as vaccine adjuvant: A systematic review. *Human Vaccines and Immunotherapeutics* 12, 159–169 (2016).
44. Aucouturier, J., Dupuis, L., Deville, S., Ascarateil, S. & Ganne, V. Montanide ISA 720 and 51: A new generation of water in oil emulsions as adjuvants for human vaccines. *Expert Review of Vaccines* 1, 111–118 (2002).
45. D'Errico, G., Ortona, O., Capuano, F. & Vitagliano, V. Diffusion coefficients for the binary system glycerol + water at 25 °C. a velocity correlation study. *J. Chem. Eng. Data* 49, 1665–1670 (2004).
46. Kretzmer, G. & Schgerl, K. Response of mammalian cells to shear stress. *Appl.*

*Microbiol. Biotechnol.* 34, 613–616 (1991).
47. Tilles, A. W., Baskaran, H., Roy, P., Yarmush, M. L. & Toner, M. Effects of oxygenation and flow on the viability and function of rat hepatocytes cocultured in a microchannel flat-plate bioreactor. *Biotechnol. Bioeng.* 73, 379–89 (2001).
48. Skylar-Scott, M. A. *et al.* Biomanufacturing of organ-specific tissues with high cellular density and embedded vascular channels. *Sci. Adv.* 5, (2019).
49. Aguado, B. A., Mulyasasmita, W., Su, J., Lampe, K. J. & Heilshorn, S. C. Improving viability of stem cells during syringe needle flow through the design of hydrogel cell carriers. *Tissue Eng. - Part A* 18, 806–815 (2012).
50. Matthews, G. *Pesticide Application Methods*. (2008).
51. Pimentel, D. & Levitan, L. Pesticides: Amounts applied and amounts reaching pests. Often, less than 0.1% of pesticides applied to crops reaches target pests. *Bioscience* 36, 86–91 (1986).
52. Pionke, H. B. & Glotfelty, D. E. Nature and extent of groundwater contamination by pesticides in an agricultural watershed. *Water Res.* 23, 1031–1037 (1989).
53. Gilliom, R. J. *Pesticides in the Nation's Streams and Ground Water, 1992–2001 Geological Survey (US)*. (2007).
54. Tang, F. H. M., Lenzen, M., McBratney, A. & Maggi, F. Risk of pesticide pollution at the global scale. *Nat. Geosci.* 14, 206–210 (2021).
55. Aktar, W., Sengupta, D. & Chowdhury, A. Impact of pesticides use in agriculture: Their benefits and hazards. *Interdiscip. Toxicol.* 2, 1–12 (2009).
56. Public Health Impact of Pesticides Used in Agriculture. *WHO* (1990).
57. Boedeker, W., Watts, M., Clausing, P. & Marquez, E. The global distribution of acute unintentional pesticide poisoning: estimations based on a systematic review. *BMC Public Health* 20, 1–19 (2020).
58. WHO | Childhood pesticide poisoning: Information for advocacy and action.
59. Pimentel, D. & Burgess, M. Environmental and economic costs of the application of pesticides primarily in the United States. in *Integrated Pest Management* 3, 47–71 (Springer Netherlands, 2014).
60. Lee, S. J. *et al.* Acute pesticide illnesses associated with off-target pesticide drift from agricultural applications: 11 states, 1998-2006. *Environ. Health Perspect.* 119, 1162–1169 (2011).
61. Brooks, N. L. *Electronic Report from the Economic Research Service Statistical Bulletin Number 974-2 Characteristics and Production Costs of U.S. Cotton Farms*. (2001).
62. Quéré, D. Non-sticking drops. *Reports Prog. Phys.* 68, 2495–2532 (2005).
63. Lafuma, A. & Quéré, D. Superhydrophobic states. *Nature Materials* 2, 457–460 (2003).
64. Richard, D. & Quéré, D. Bouncing water drops. *Europhys. Lett.* 50, 769–775 (2000).

65. Clanet, C., Béguin, C., Richard, D. & Quéré, D. Maximal deformation of an impacting drop. *J. Fluid Mech.* 517, 199–208 (2004).
66. Liu, Y. *et al.* Pancake bouncing on superhydrophobic surfaces. *Nat. Phys.* 10, 515–519 (2014).
67. Bird, J. C., Dhiman, R., Kwon, H. M. & Varanasi, K. K. Reducing the contact time of a bouncing drop. *Nature* 503, 385–388 (2013).
68. Deng, X., Schellenberger, F., Papadopoulos, P., Vollmer, D. & Butt, H. J. Liquid drops impacting superamphiphobic coatings. *Langmuir* 29, 7847–7856 (2013).
69. Duez, C., Ybert, C., Clanet, C. & Bocquet, L. Making a splash with water repellency. *Nat. Phys.* 3, 180–183 (2007).
70. De Ruiter, J., Oh, J. M., Van Den Ende, D. & Mugele, F. Dynamics of collapse of air films in drop impact. *Phys. Rev. Lett.* 108, 074505 (2012).
71. Bartolo, D., Josserand, C. & Bonn, D. Retraction dynamics of aqueous drops upon impact on non-wetting surfaces. *J. Fluid Mech.* 545, 329–338 (2005).
72. D. Nuyttens, M. De Schampheleire, P. Verboven, E. Brusselman & D. Dekeyser. Droplet Size and Velocity Characteristics of Agricultural Sprays. *Trans. ASABE* 52, 1471–1480 (2009).
73. Dorr, G. J. *et al.* A comparison of initial spray characteristics produced by agricultural nozzles. *Crop Prot.* 53, 109–117 (2013).
74. Kooij, S., Sijs, R., Denn, M. M., Villermaux, E. & Bonn, D. What Determines the Drop Size in Sprays? *Phys. Rev. X* 8, 031019 (2018).
75. Whitford, F. & Lindner, G. *Adjuvants and the Power of the Spray Droplet Droplet Improving the Performance of Pesticide Applications.*
76. Gaskin, R. E., Steele, K. D. & Forster, W. A. Characterising plant surfaces for spray adhesion and retention. *New Zeal. Plant Prot.* 58, 179–183 (2005).
77. Zhang, X. & Basaran, O. A. Dynamic Surface Tension Effects in Impact of a Drop with a Solid Surface. *J. Colloid Interface Sci.* 187, 166–178 (1997).
78. Aytouna Denis Bartolo AE Gerard Wegdam AE Daniel Bonn AE Salima Rafaı, M. A. Impact dynamics of surfactant laden drops: dynamic surface tension effects. *Springer* (2010). doi:10.1007/s00348-009-0703-9
79. Hoffman, H., Sijs, R., De Goede, T. & Bonn, D. Controlling droplet deposition with surfactants. *Phys. Rev. Fluids* 6, 033601 (2021).
80. Butler Ellis, M. C., Tuck, C. R. & Miller, P. C. H. How surface tension of surfactant solutions influences the characteristics of sprays produced by hydraulic nozzles used for pesticide application. *Colloids Surfaces A Physicochem. Eng. Asp.* 180, 267–276 (2001).
81. Sijs, R. & Bonn, D. The effect of adjuvants on spray droplet size from hydraulic nozzles. *Pest Manag. Sci.* 76, 3487–3494 (2020).
82. Krogh, K. A., Halling-Sørensen, B., Mogensen, B. B. & Vejrup, K. V. Environmental properties and effects of nonionic surfactant adjuvants in

pesticides: a review. *Chemosphere* 50, 871–901 (2003).
83. Mesnage, R., Bernay, B. & Séralini, G. E. Ethoxylated adjuvants of glyphosate-based herbicides are active principles of human cell toxicity. *Toxicology* 313, 122–128 (2013).
84. Castro, M. J. L., Ojeda, C. & Cirelli, A. F. Advances in surfactants for agrochemicals. doi:10.1007/s10311-013-0432-4
85. Mesnage, R., Defarge, N., Spiroux de Vendômois, J. & Séralini, G. E. Potential toxic effects of glyphosate and its commercial formulations below regulatory limits. *Food Chem. Toxicol.* 84, 133–153 (2015).
86. Myers, J. P. *et al.* Concerns over use of glyphosate-based herbicides and risks associated with exposures: A consensus statement. *Environ. Heal. A Glob. Access Sci. Source* 15, 1–13 (2016).
87. Mesnage, R. & Antoniou, M. N. Ignoring Adjuvant Toxicity Falsifies the Safety Profile of Commercial Pesticides. *Front. Public Heal.* 5, 361 (2018).
88. Mesnage, R., Benbrook, C. & Antoniou, M. N. Insight into the confusion over surfactant co-formulants in glyphosate-based herbicides. *Food Chem. Toxicol.* 128, 137–145 (2019).
89. Bloomberg. Bayer's Roundup Costs Could Top $16 Billion as Provisions Mount - Bloomberg.
90. Smith, D. B., Askew, S. D., Morris, W. H., Shaw, D. R. & Boyette, M. Droplet Size and Leaf Morphology Effects On Pesticide Spray Deposition. *Trans. ASAE* 43, 255- (2000).
91. Bergeron, V. Designing intelligent fluids for controlling spray applications. *Comptes Rendus Phys.* 4, 211–219 (2003).
92. Riseman, A. & Frostad, J. M. Quantifying the effect of extensional rheology on the retention of agricultural sprays. *Phys. Fluids* 33, 032107 (2021).
93. Patel, M. K. Technological improvements in electrostatic spraying and its impact to agriculture during the last decade and future research perspectives – A review. *Eng. Agric. Environ. Food* 9, 92–100 (2016).
94. Salcedo, R. *et al.* Evaluation of leaf deposit quality between electrostatic and conventional multi-row sprayers in a trellised vineyard. *Crop Prot.* 127, 104964 (2020).
95. Damak, M., Hyder, M. N. & Varanasi, K. K. Enhancing droplet deposition through in-situ precipitation. *Nat. Commun. 2016 71* 7, 1–9 (2016).
96. Bogran, C. E., Ludwig, S. & Metz, B. Using Oils As Pesticides. (2006).
97. Pesticides in the Modern World-Pesticides Use and Management. (2011).
98. EPA Office of Pesticide Programs, U. Fact Sheet for Flower and Vegetable Oils.
99. EPA Office of Pesticide Programs, U. Biopesticides Fact Sheet for Plant Oils.
100. *Vegetable Oils in Food Technology: Composition, Properties and Uses.* (John Wiley & Sons, 2011).

101. Cornish, A., Battersby, N. S. & Watkinson, R. J. Environmental fate of mineral, vegetable and transesterified vegetable oils. *Pestic. Sci.* 37, 173–178 (1993).
102. Pavela, R. Limitation of Plant Biopesticides. *Adv. Plant Biopestic.* 347–359 (2014). doi:10.1007/978-81-322-2006-0_17
103. da Silva, I. M. *et al.* Selectivity of the botanical compounds to the pollinators Apis mellifera and Trigona hyalinata (Hymenoptera: Apidae). *Sci. Reports 2020 101* 10, 1–8 (2020).
104. Zheng, L. *et al.* Bounce Behavior and Regulation of Pesticide Solution Droplets on Rice Leaf Surfaces. *J. Agric. Food Chem* 66, 16 (2018).
105. Blanken, N., Saleem, M. S., Antonini, C. & Thoraval, M. J. Rebound of self-lubricating compound drops. *Sci. Adv.* 6, eaay3499 (2020).
106. Gao, P. & Feng, J. J. Spreading and breakup of a compound drop on a partially wetting substrate. *J. Fluid Mech.* 682, 415–433 (2011).
107. Blanken, N., Saleem, M. S., Thoraval, M.-J. & Antonini, C. Impact of compound drops: a perspective. *Curr. Opin. Colloid Interface Sci.* (2020). doi:10.1016/j.cocis.2020.09.002
108. Liu, D. & Tran, T. The ejecting lamella of impacting compound droplets. *Appl. Phys. Lett.* 115, 073702 (2019).
109. Liu, H. R., Zhang, C. Y., Gao, P., Lu, X. Y. & Ding, H. On the maximal spreading of impacting compound drops. *J. Fluid Mech.* 854, R6 (2018).
110. Liu, D. & Tran, T. Emergence of two lamellas during impact of compound droplets. *Appl. Phys. Lett.* 112, 203702 (2018).
111. Baker, B. P., Grant, J. A. & Malakar-Kuenen, R. Soybean Oil Profile Soybean Oil Profile Active Ingredient Eligible for Minimum Risk Pesticide Use.
112. Lee, J. B. *et al.* Universal rescaling of drop impact on smooth and rough surfaces. *J. Fluid Mech.* 786, R41–R411 (2016).
113. Biance, A.-L. & Lagubeau, G. On the Elasticity of an Inertial Liquid Shock. *Artic. J. Fluid Mech.* 554, 47–66 (2006).
114. Gao, L. & McCarthy, T. J. Wetting 101°†. *Langmuir* 25, 14105–14115 (2009).
115. David Smith, J. *et al.* Droplet mobility on lubricant-impregnated surfaces. *Soft Matter* 9, 1772–1780 (2013).
116. Sharma, P. K. & Dixit, H. N. Energetics of a bouncing drop: Coefficient of restitution, bubble entrapment, and escape. *Phys. Fluids* 32, 112107 (2020).
117. Carlson, A., Kim, P., Amberg, G. & Stone, H. A. Short and long time drop dynamics on lubricated substrates. *EPL* 104, 34008 (2013).
118. Courbin, L., Bird, J. C., Reyssat, M. & Stone, H. A. Dynamics of wetting: From inertial spreading to viscous imbibition. *J. Phys. Condens. Matter* 21, (2009).
119. CO2 emissions - Our World in Data. Available at: https://ourworldindata.org/co2-emissions. (Accessed: 14th October 2021)
120. AR5 Climate Change 2014: Mitigation of Climate Change — IPCC. Available at:

https://www.ipcc.ch/report/ar5/wg3/. (Accessed: 14th October 2021)
121. AVoided Emissions and geneRation Tool (AVERT) | US EPA. Available at: https://www.epa.gov/avert. (Accessed: 14th October 2021)
122. Epa, U. & Change Division, C. Inventory of U.S. Greenhouse Gas Emissions and Sinks: 1990-2019 – Main Text - Corrected Per Corrigenda, Updated 05/2021. (1990).
123. Notz, R. J., Tönnies, I., McCann, N., Scheffknecht, G. & Hasse, H. CO2 Capture for Fossil Fuel-Fired Power Plants. *Chem. Eng. Technol.* 34, 163–172 (2011).
124. Chao, C., Deng, Y., Dewil, R., Baeyens, J. & Fan, X. Post-combustion carbon capture. *Renew. Sustain. Energy Rev.* 138, 110490 (2021).
125. Post-Combustion CO2 Capture | netl.doe.gov. Available at: https://netl.doe.gov/coal/carbon-capture/post-combustion. (Accessed: 13th October 2021)
126. Samanta, A., Zhao, A., Shimizu, G. K. H., Sarkar, P. & Gupta, R. Post-Combustion CO2 Capture Using Solid Sorbents: A Review. *Ind. Eng. Chem. Res.* 51, 1438–1463 (2011).
127. Wang, M., Lawal, A., Stephenson, P., Sidders, J. & Ramshaw, C. Post-combustion CO2 capture with chemical absorption: A state-of-the-art review. *Chem. Eng. Res. Des.* 89, 1609–1624 (2011).
128. Luis, P. & Bruggen, B. Van der. The role of membranes in post-combustion CO2 capture. *Greenh. Gases Sci. Technol.* 3, 318–337 (2013).
129. Zhao, S. *et al.* Status and progress of membrane contactors in post-combustion carbon capture: A state-of-the-art review of new developments. *J. Memb. Sci.* 511, 180–206 (2016).
130. Mattisson, T., Lyngfelt, A. & Cho, P. The use of iron oxide as an oxygen carrier in chemical-looping combustion of methane with inherent separation of CO2. *Fuel* 80, 1953–1962 (2001).
131. Ben-Mansour, R. *et al.* Carbon capture by physical adsorption: Materials, experimental investigations and numerical modeling and simulations – A review. *Appl. Energy* 161, 225–255 (2016).
132. Song, C., Liu, Q., Deng, S., Li, H. & Kitamura, Y. Cryogenic-based CO2 capture technologies: State-of-the-art developments and current challenges. *Renew. Sustain. Energy Rev.* 101, 265–278 (2019).
133. Giordano, L., Roizard, D. & Favre, E. Life cycle assessment of post-combustion CO2 capture: A comparison between membrane separation and chemical absorption processes. *Int. J. Greenh. Gas Control* 68, 146–163 (2018).
134. Savile, C. K. & Lalonde, J. J. Biotechnology for the acceleration of carbon dioxide capture and sequestration. *Curr. Opin. Biotechnol.* 22, 818–823 (2011).
135. Ho, S. H., Chen, C. Y., Lee, D. J. & Chang, J. S. Perspectives on microalgal CO2-emission mitigation systems — A review. *Biotechnol. Adv.* 29, 189–198 (2011).

136. Mohd Shariff, A. *et al.* Factors affecting CO2 absorption efficiency in packed column: A review Author's personal copy Review Factors affecting CO 2 absorption efficiency in packed column: A review. doi:10.1016/j.jiec.2012.05.013
137. Iso, Y., Huang, J., Kato, M., Matsuno, S. & Takano, K. Numerical and Experimental Study on Liquid Film Flows on Packing Elements in Absorbers for Post-combustion CO2 Capture. *Energy Procedia* 37, 860–868 (2013).
138. Singh, R. K., Galvin, J. E. & Sun, X. Multiphase flow studies for microscale hydrodynamics in the structured packed column. *Chem. Eng. J.* 353, 949–963 (2018).
139. Sebastia-Saez, D., Gu, S., Ranganathan, P. & Papadikis, K. Micro-scale CFD modeling of reactive mass transfer in falling liquid films within structured packing materials. *Int. J. Greenh. Gas Control* 33, 40–50 (2015).
140. Agbonghae, E. O., Hughes, K. J., Ingham, D. B., Ma, L. & Pourkashanian, M. Optimal Process Design of Commercial-Scale Amine-Based CO2 Capture Plants. *Ind. Eng. Chem. Res.* 53, 14815–14829 (2014).
141. Husebye, J., Brunsvold, A. L., Roussanaly, S. & Zhang, X. Techno Economic Evaluation of Amine based CO2 Capture: Impact of CO2 Concentration and Steam Supply. *Energy Procedia* 23, 381–390 (2012).
142. GLOBAL STATUS OF CCS 2020.
143. Cho, M., Lee, S., Choi, M. & Lee, J. W. Novel Spray Tower for CO2 Capture Using Uniform Spray of Monosized Absorbent Droplets. *Ind. Eng. Chem. Res.* 57, 3065–3075 (2018).
144. and, J. K. & Aroonwilas*, A. Performance of Spray Column for CO2 Capture Application. *Ind. Eng. Chem. Res.* 47, 145–153 (2007).
145. Xu, Y. *et al.* Numerical simulation of aqueous ammonia-based CO2 absorption in a sprayer tower: An integrated model combining gas-liquid hydrodynamics and chemistry. *Appl. Energy* 211, 318–333 (2018).
146. Wan, Z. & Li, Y. Numerical study of the falling film wettability and heat transfer on the inclined plates with different corrugated structures. *Asia-Pacific J. Chem. Eng.* 16, e2664 (2021).
147. Khakharia, P., Kvamsdal, H. M., Da Silva, E. F., Vlugt, T. J. H. & Goetheer, E. Field study of a Brownian Demister Unit to reduce aerosol based emission from a Post Combustion CO2 Capture plant. *Int. J. Greenh. Gas Control* 28, 57–64 (2014).
148. Rahimi, R. & Abbaspour, D. Determination of pressure drop in wire mesh mist eliminator by CFD. *Chem. Eng. Process. Process Intensif.* 47, 1504–1508 (2008).
149. Parker, K. R. Applied electrostatic precipitation. 521 (1997).
150. Damak, M. & Varanasi, K. K. Electrostatically driven fog collection using space charge injection. *Sci. Adv.* 4, (2018).
151. Choi, M., Cho, M. & Lee, J. W. Empirical formula for the mass flux in chemical

absorption of CO2 with ammonia droplets. *Appl. Energy* 164, 1–9 (2016).
152. Epa. Wet Electrostatic Precipitator (ESP) - Wire Pipe Type.
153. Reynolds, J. P., Theodore, L. & Marino, J. Calculating Collection Efficiencies for Electrostatic Precipitators. *J. Air Pollut. Control Assoc.* 25, 610–616 (1975).
154. Turner, J. H. *et al.* Electrostatic Precipitators. (1999).
155. IECM Technical Documentation: Amine-based Post-Combustion CO 2 Capture.
156. Keith, D. W., Holmes, G., St. Angelo, D. & Heidel, K. A Process for Capturing CO2 from the Atmosphere. *Joule* 2, 1573–1594 (2018).
157. Analysis, Synthesis and Design of Chemical Processes - Richard Turton, Richard C. Bailie, Wallace B. Whiting, Joseph A. Shaeiwitz - Google Books. Available at: https://books.google.com/books?hl=en&lr=&id=kWXyhVXztZ8C&oi=fnd&pg=PT3&dq=%5B1%5D+Turton,+R.+et+al.+Analysis,+Synthesis,+and+Design+of+Chemical+Processes.+Prentice+Hall,+2009.&ots=p_lVsHvQvG&sig=ExBigZieQSrpwzJE26pzjO8KtaQ#v=onepage&q&f=false. (Accessed: 15th October 2021)
158. Woodard, M. K. Stationary Source Control Techniques Document for Fine Particulate Matter. (1998).